EARTH SCIENCES
RESEARCH JOURNAL

Earth Sci. Res. J. Vol. 25, No. 2 (June, 2021): 139-156

UNIVERSIDAD NACIONAL DE COLOMBIA

MINERALOGY

Mineralogy and fluid inclusions of the Cunas emerald mine, Maripí - Boyacá, Colombia

Fernando Helí Romero Ordóñez[1], Andrés Felipe González-Durán[2*], Javier García-Toloza[2], Jimmy Rotlewicz Cohen[3], Carlos Julio Cedeño Ochoa[2], Holman Rolando Alvarado González[2], Luis Gabriel Angarita Sarmiento[2]

[1]Departamento de Geociencias, Universidad Nacional de Colombia. Bogotá. Av. Carrera 30 # 45-03

[2]Technological Development Center for the Colombian Emeralds CDTEC. Bogotá. Calle 12B #6-82

[3]Gemtec S.A.S. Bogotá. Av. Jiménez 5-43 Of. 902

*Corresponding author: geologist@gemlabcdtec.com

ABSTRACT

The Cunas mine is currently one of the major producers of fine emeralds in Colombia; its emeralds typically display a magnificent green hue, which is highly appreciated globally. The mineralization is found in vanadium-rich black shales of the Muzo formation. Emeralds occur in pockets within hydrothermal veins and breccias, mainly consisting of calcite, dolomite, albite, quartz, minor pyrite, parisite-(Ce), and fluorite. Hydrothermal alteration is pervasive and dominated by albitization and carbonatization. Emerald-hosted fluid inclusions are highly abundant and remarkably large and complex. Poly-phase inclusions are ubiquitous, occur both in emeralds and gangue minerals, and consist of two daughter crystals (typically halite and calcite or siderite; exceptionally parisite-(Ce)), a liquid brine, a CO_2-N_2-CH_4-rich gas bubble, and occasionally minor liquid CO_2. Vapor-rich inclusions were observed in quartz, and two-phase inclusions were identified in calcite and dolomite, thus suggesting a complex fluid evolution. Microthermometry analysis indicates that emerald-forming fluids were trapped at relatively low temperature ~260-340°C and pressure ~850-2400 bar, with relatively high density 1.03 g/cm³, and elevated salinity ~39 wt% NaCl eq.; other aqueous components detected include $CaCl_2$, KCl, and $FeCl_2$. Based on these data, authors propose the emerald mineralization at the Cunas mine was originated by the mixing of two hydrothermal fluids of different sources; one fluid with high salinity derived from evaporite dissolution, responsible for the albitization of the host rocks; the second is a calcium-rich fluid evolved from connate waters, which was equilibrated by the interaction with calcareous and organic-rich wall rocks. As a result, emerald mineralization took place at structurally favorable sites proper for fluid mixing. The described geological and physicochemical features for the Cunas mine agree with epigenetic sediment-hosted mineralization —Colombian-type— formed by the circulation and mixing of relatively low-temperature non-magmatic fluids.

Keywords: Emeralds; Sediment-hosted; Colombian-type; Gemstones

Mineralogía e inclusiones fluidas de la mina de esmeraldas “Cunas”, Maripí, Boyacá, Colombia

RESUMEN

La mina Cunas es actualmente una de las principales productoras de esmeraldas de alta calidad en Colombia. Sus gemas se caracterizan por un intenso tono verde muy apreciado en el mercado mundial. La mineralización se encuentra en lodolitas negras, ricas en vanadio, de la formación Muzo. Las esmeraldas se encuentran al interior de venas hidrotermales y brechas, compuestas principalmente por calcita, dolomita, albita, cuarzo y, en menor medida, pirita, parisita- (Ce) y fluorita. La alteración hidrotermal asociada es pervasiva y está dominada por la albitización y la carbonatización. Las inclusiones fluidas alojadas en esmeraldas son muy abundantes, de gran tamaño y alta complejidad. Las inclusiones fluidas polifásicas son ubicuas, ocurren tanto en esmeraldas como en minerales de ganga, y generalmente están compuestas por dos cristales hijos (típicamente halita y calcita o siderita; excepcionalmente parisita- (Ce)), una salmuera, un gas rico en CO_2-N_2-CH_4, y ocasionalmente CO_2 líquido. También se observaron inclusiones ricas en vapor en cuarzo y se identificaron inclusiones bifásicas en calcita y dolomita, lo que sugiere una evolución de fluido compleja. El análisis de microtermometría indica que los fluidos formadores de esmeraldas quedaron atrapados a una temperatura relativamente baja ≈ 260-340 ° C y una presión ≈ 875-2400 bar, con una densidad relativamente alta —1,03 g / cm³— y una salinidad elevada de 39% NaCl eq. peso; otros componentes acuosos detectados fueron $CaCl_2$, KCl y $FeCl_2$. Con base en estos datos, los autores proponen que la mineralización de esmeraldas en la mina Cunas se originó por la mezcla de dos fluidos hidrotermales de diferentes fuentes. Un fluido con alta salinidad derivado de la disolución de evaporitas, el cual es responsable de la albitización de las rocas hospedantes. El segundo es un fluido rico en calcio derivado de aguas connadas, que fue equilibrado por la interacción con rocas calcáreas y carbonosas. Como resultado, la mineralización de esmeraldas ocurrió en sitios estructuralmente favorables donde se promovió la mezcla de fluidos. Las características geológicas y fisicoquímicas descritas para la mina Cunas, están de acuerdo con una mineralización epigenética alojada en sedimentos "tipo colombiano" formada por la circulación y mezcla de fluidos no magmáticos de temperatura relativamente baja.

Palabras clave: esmeraldas; tipo Colombia; hospedado en sedimentos; gemas

Record
Manuscript received: 29/08/2020
Accepted for publication: 05/02/2021

How to cite item
Romero-Ordóñez, F. H., González-Durán, A. F., García-Toloza, J., Rotlewicz-Cohen, J., Cedeño-Ochoa, C. J., Alvarado-González, H. R., & Angarita-Sarmiento, L. G. (2021). Mineralogy and fluid inclusions of the Cunas emerald mine, Maripí - Boyacá, Colombia. *Earth Sciences Research Journal*, 25(2), 139-156. DOI: https://doi.org/10.15446/esrj.v25n2.90210

ISSN 1794-6190 e-ISSN 2339-3459

https://doi.org/10.15446/esrj.v25n2.90210

Introduction

The geological setting of the Colombian emerald deposits is remarkably unique in comparison with other locations. The mineralization is restricted to Lower Cretaceous marine rocks and linked to the circulation of non-magmatic hydrothermal fluids (Branquet *et al.*, 1999; Ortega 2007; Giuliani *et al.*, 2015; Terraza, 2019). Despite sediment-hosted emerald mineralization having been reported in Canada (Hewton *et al.*, 2013) and United States (e.g. Keith *et al.*, 2002), gem-quality emeralds are only being extracted in Colombia. On the other hand, other fine emerald deposits worldwide are associated with igneous or metamorphic processes (Groat *et al.*, 2008; Giuliani *et al.*, 2019).

Additionally, the source of the chemical components required for the emerald formation —beryllium, chromium, vanadium, aluminum, and silicon— is thought to be a single set of rocks in the Colombian deposits: the black shale strata; whereas in other countries more than one rock type is involved. For instance, the emerald deposits of the Kafubu area in Zambia, are formed by the interaction of schist —derived from ultramafic rocks enriched with iron, chromium, and vanadium— with beryllium-bearing pegmatites (Zwaan *et al.*, 2005).

In Colombia, emerald deposits can be divided into two mining belts (Eastern and Western). The districts of Chivor, Gachalá, and Macanal are grouped in the Eastern belt; whereas Muzo — Quipama, Maripí, Coscuez, Peñas Blancas and Yacopí — La Palma are part of the Western area. The mineralization style is roughly the same in both belts, however, some significant differences can be noticed regarding the host rocks, mineral assemblages, and the structural setting (Branquet *et al.,* 1999; Terraza, 2019). The Maripí district is a prominent emerald mining area composed of several mines, including La Pita, Cunas, Totumos, Españoles, and Polveros (Figure 1) (Reyes *et al.,* 2006), and it is currently the second-largest emerald producer in Colombia.

The study of fluid inclusions has yielded crucial information about the genesis of the Colombian emeralds. For instance, Roedder (1963) reported the presence of various salts, CO_2 and calcite, in a pioneering study of microthermometric data of fluid inclusions, suggesting a hypersaline mineralizing fluid derived from the interaction with evaporitic beds. Further studies —putting together isotopic and chemical approaches— have shown the presence, in all the deposits, of primary three-phase (halite, brine, and gas) or multiphase fluid inclusions containing CO_2 and N_2 in the vapor phase (Kozlowski *et al.*, 1988; Giuliani *et al.*, 1990; Romero, 1993; Ottaway, 1994; Giuliani *et al.*, 2000; Banks *et al.*, 2000). Halite, sylvite, sulfate and chloride compounds, with cations (namely Ca^{2+}, Fe^{2+}, Mn^{2+}, and Cr^{3+}) were identified. The microthermometric data also indicate a range of salinity from 38 to 50 wt% NaCl eq.; average homogenization temperatures are 250° C for the Eastern belt and 380°C for the Western belt; and high density —1.20-1.22 g/cm³— hydrothermal solutions (Kozlowski *et al.*, 1988; Giuliani *et al.*, 1990; Romero, 1993; Ottaway, 1994; Giuliani *et al.*, 2000; Banks *et al.*, 2000). Based on these results, an unusual sediment-hosted model involving non-magmatic hydrothermal brines has been proposed as the mechanism responsible for the emerald mineralization (Giuliani *et al.*, 2019).

Despite the extensive available information dealing with the geology and geochemistry of Muzo and other Colombian emerald districts, few data have been published regarding the Maripí mines. In this study, we documented the main mineralogical features of the Cunas mine as well as data fluid inclusions trapped in the emerald crystals, aiming to unravel the physicochemical conditions that gave rise to the emerald mineralization. Distinct spectroscopic and mineralogical techniques were applied, and the results were compared with available data from other emerald mines in Colombia and other countries.

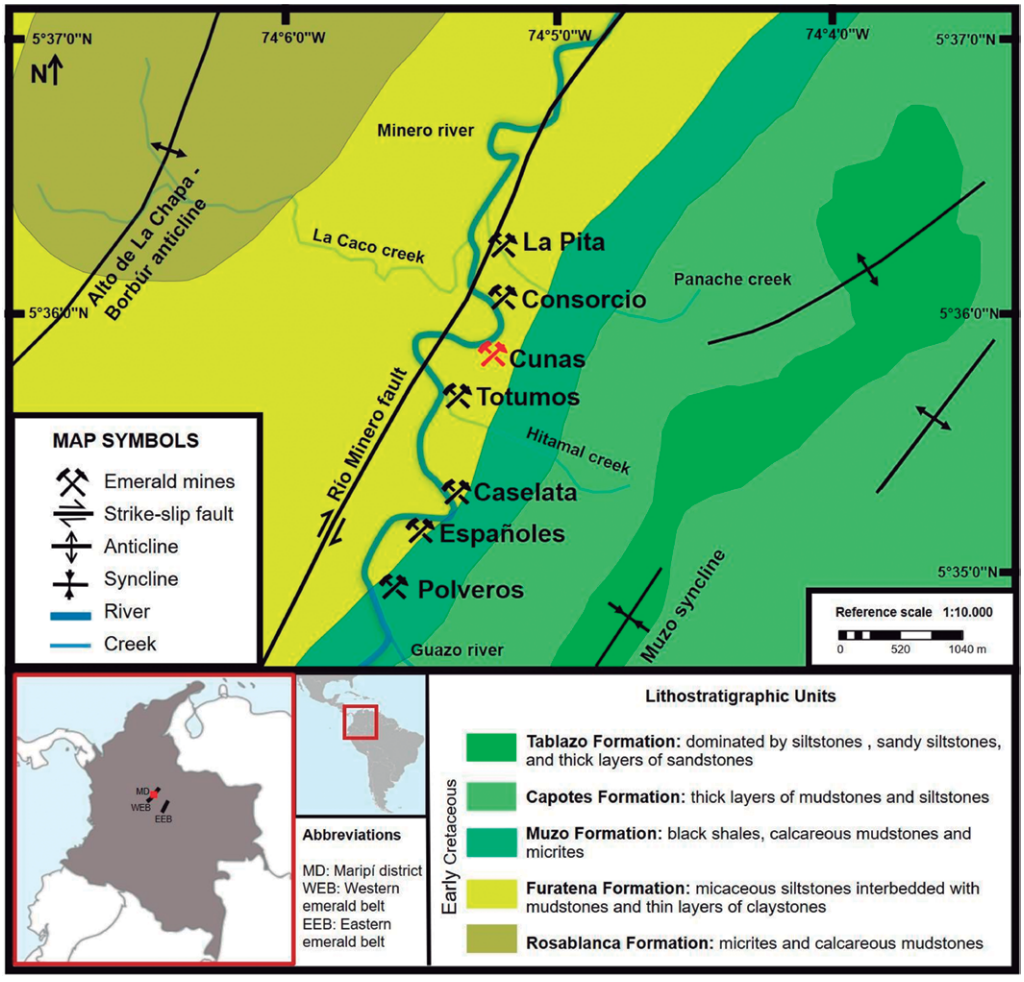

Figure 1. Geological map of the Maripí emerald district in Colombia. Adapted from Reyes et al. (2006).

Geological framework

The Colombian emerald deposits are located in the Eastern Andean Cordillera, especially in the area of Boyacá. The Eastern Cordillera has arisen as a result of multiple and protracted tectonic processes involving pre-Cretaceous basement and Mesozoic —Cenozoic basins. Particularly, the sedimentary record evidences Early Cretaceous rifting and thermal subsidence that led to the extensive accumulation of marine-dominated strata. Subsequent Late Cretaceous crustal shortening gave rise to a shift in the structural setting of the sedimentation, where a compressional style predominated. Paleocene—Oligocene compressional uplifts promoted the generation of sub-basins (Magdalena hinterland basin and Llanos foreland basin) and the sedimentation was significantly influenced by continental inputs. Further uplifting caused the exhumation of a Cordillera dominated by sedimentites between ~13 and 3 Ma (Van der Hammen, 1958; Cooper *et al.*, 1995; Mojica, 1995; Acosta *et al.*, 2007, Horton *et al.*, 2020; Mora *et al.,* 2020).

The two emerald belts lie on Lower Cretaceous marine strata. In the Western Emerald Belt, the main lithostratigraphic units include the Rosablanca Formation, which predominantly comprises dark grey and black limestones, and it is overlain by the Furatena Formation, which consists of a series of claystones and siltstones; followed by the Muzo Formation, consisting of up to 300 meters of calcareous mudstones, black shales, and minor micrites; the Capotes Formation, consisting of a thick succession of claystones and siltstones, and finally, a succession dominated by siltstones, sandy siltstones and thick layers of sandstones from the Tablazo Formation (Figure 2) (Reyes *et al.*, 2006; Terraza 2019).

In the Muzo - Maripí area, the emerald mineralization is restricted to the Hauterivian-Barremian (115-125 Ma) calcareous layers of the Muzo Formation (Reyes *et al.*, 2006; Terraza 2019); these rocks are mostly organic-rich (Beus & Mineev, 1972; Mantilla *et al.*, 2007) and made up of quartz, paragonite, muscovite (2M1 illite), microcline, and minor calcite, pyrite, baryte, with traces of clay minerals such as pyrophyllite, dickite, chlorite, and kaolinite (Gonzalez-Duran *et al.* 2019). The emeralds are found in nodules, lenses and pockets within veins and hydraulic breccias. The mineralogical and isotopic features are generally similar in all mines, with small differences possibly related to local fluid-rock interactions (Giuliani *et al.*, 1995; Romero, 1998; Pignatelli *et al.*, 2015; Niño, 2017). The typical mineral assemblage reported in the Maripí district includes calcite, dolomite, albite, pyrite and emerald (Mantilla *et al.*, 2007; Castaño *et al.*, 2019).

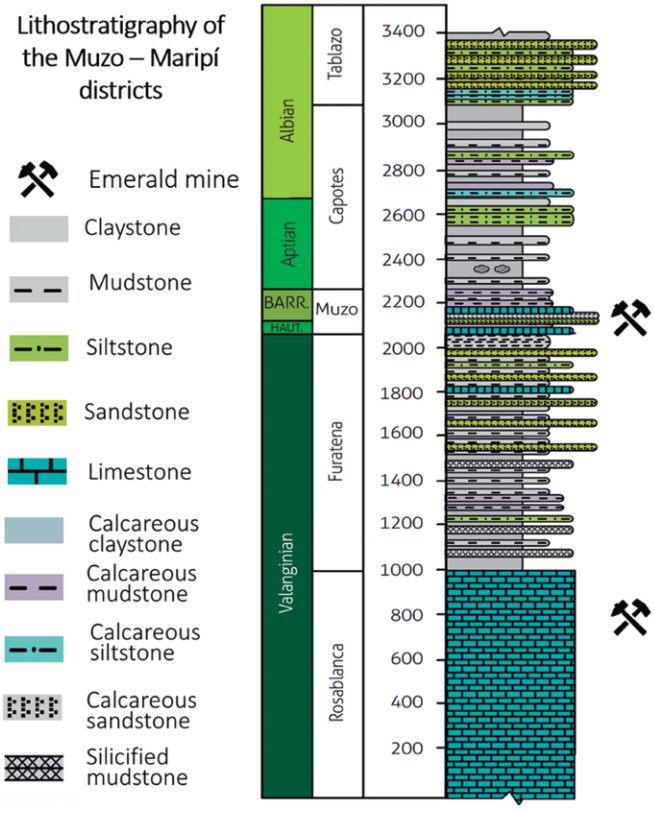

Figure 2. Simplified stratigraphic column of the Muzo - Maripí mining area; modified from Terraza (2019)

The Maripí district is 6 km apart from the main Muzo mining area. The Cunas mine is located northwestern of the Maripí town, next to the channel of the Minero River and southern from the Panache creek (Figure 3A). La Pita, Consorcio, Españoles, Polveros, Caselata, Bonanza, and Totumos mines are also part of the Maripí mining district, which extends more than 6 kilometers conforming an NNE gemstone belt (Figure 1).

In terms of structural framework, the area is dominated by compressive structures developed during a tectonic phase that occurred before the major uplift of the Eastern Cordillera (Branquet *et al.*, 1999). The Cunas mine is situated on the eastern limb of the Alto La Chapa-Borbur Anticline (Reyes *et al.*, 2006). Puerto *et al.* (2012) indicated that the fertile veins in the La Pita mine are predominantly oriented N10E to N40E, and suggested a genetic link with the Río Minero fault, which is a major dextral strike-slip structure (Reyes *et al.*, 2006). García-Toloza *et al.* (2018) described emerald-bearing veins oriented N30E to N50E in the deepest levels of the Cunas mine, and reported that the mineralization is intimately related with hydrothermal breccias and the re-opening of previous antitaxial veins. Valls (2017) pointed out the emerald mineralization appears to be controlled by fault junctions, suggesting that mineralization took place where major NNE-SSW fault systems (in particular the Río Minero fault) intersected secondary E-W structures.

Some authors have proposed different structural models for the mineralization at the western emerald belt; Branquet *et al.* (1999) suggested that the mineralizing fluids migrated through thrust and decollement fault systems during a compressional tectonic event; whereas, Terraza (2019) stated that the mineralization is associated with a different array of mesoscopic structures and ruled out a genetical relationship with fault zones. Different sources argue that early tectonics promoted fragile deformation controlled by a penetrative strain regime; this eventually led to a series of events: fluid overpressure, infill of preexisting fractures, and further hydraulic brecciation (Ingeominas & Mora, 2005; Terraza, 2019).

On the other hand, Pignatelli *et al.* (2015) suggested that the emerald and trapiche formation are associated with thrust propagation and subsequent fluid decompression, a structurally controlled process that took place at the core of anticlines. González-Duran *et al.* (2019) also report that emerald mineralization in the La Pava mine (Muzo-Quipama district) is associated with anticlinal structures; likewise, Ingeominas & Mora (2005) suggest a genetic link for euclase and emerald mineralization with an anticline fold in the La Marina mine (6 km north from Cunas).

Multiple ages have been proposed for the emerald mineralization in the Western Belt. Firstly, Cheilletz *et al.* (1994) reported an Ar^{40}/Ar^{39} age in green mica of 32 ± 3 and 36 ± 3 Ma; secondly, Romero *et al.* (2000) dated emeralds through the Rb^{87}/Sr^{86} method and yielded an age of 67 Ma; thirdly, Mantilla *et al.* (2007) through the Re-Os method, obtained an age of 12.4 ± 0.9 Ma; and finally, Svadlenak (2015) reported ages of 62.05 ± 0.63, 30.25 ± 0.25, and 30.24 ± 0.06 Ma through Ar^{40}/Ar^{39} analysis in micas. The data are highly dispersive, and consequently there are no conclusive statements for the mineralization timing. Yet there is no geochronological data for any deposit in the Maripí area.

Methods

Twenty rock samples, with consecutive codes RC_01 to RC_20, were collected from the Cunas mine and subsequently studied via petrographic studies. The thin sections were observed under reflected and transmitted light. These analyses were performed in an Olympus BX-51 microscope at the Technological Development Center for the Colombian Emeralds (CDTEC). Additionally, twenty-five optimal hexagonal emerald crystals —collected in-situ by CDTEC— were selected to be studied through multiple spectroscopic and gemological techniques at the CDTEC gemological facilities. The crystals are named with the consecutive codes EC_01 to EC_25.

The standard gemological study consisted of examination of the twenty-five rough emeralds (EC_01 to EC_25) as well as three cut stones (CS_1, CS_2, and CS_3) through a KRUSS refractometer, polariscope, Chelsea Filter (GEM-A), and short-wavelength (365 nm) ultraviolet light. For spectroscopic procedures, some crystals were cut and polished to form oriented plates;

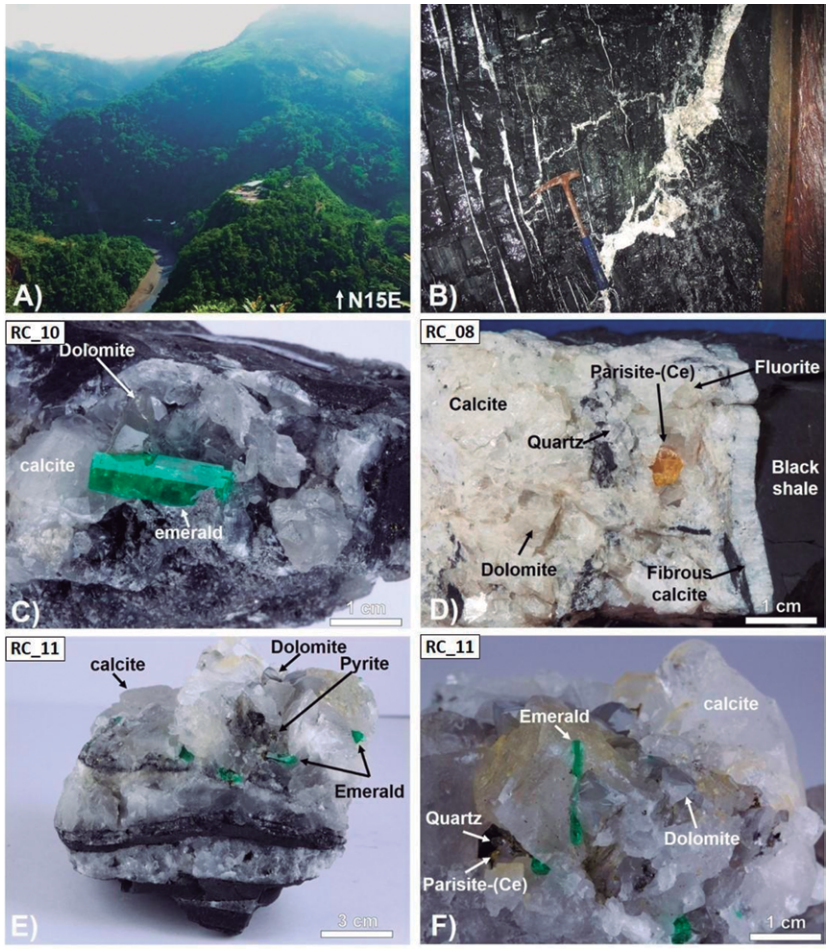

Figure 3. General aspects of the Cunas mineralization. A) Panoramic view of the Cunas mining camp and the Minero River. B) Steeply dipping black shales from a productive zone. The white veins are made up of carbonates ± emerald, hammer for scale. C) Hand sample of a black shale crosscut by a calcite-dolomite-emerald vein. D) Typical mineral assemblage from a productive zone. The fibrous calcite is part of a previous hydrothermal event, and its fibrous habit indicates an antitaxial regime. On the other hand, the rhombohedral carbonates (calcite - dolomite), parisite-(Ce), quartz, and fluorite exhibit euhedral shapes as a result of syntaxial growing. E) Hand specimen displaying an array of sub-parallel veins and drusiform growing. The emeralds are found as hexagonal crystals in the presence of calcite, dolomite, and pyrite. F) Close-up view of a pocket containing calcite —typically described as —peach skin— by the local miners—, dolomite, parisite-(Ce), quartz, and emerald. Note the largest emerald is a double terminated crystal.

two directions were considered: parallel and perpendicular planes to the crystallographic c-axis. For comparison purposes, we also analyzed three rough emerald samples from Zambia. The microscopy of the crystals and solid inclusions was carried out through a Leica gemological microscope coupled with System Eckhorst, Zeiss-Stemi 508 optics with a maximum magnification of 50x and eyepieces with 25x magnification. Additionally, an AXXIO Zoom V16 microscope was used to measure inclusions and photography acquisition.

Infrared spectra (FT-IR) of the twenty-five emeralds were collected using a Nicolet 6700 Fourier Transform Infrared spectrometer with a DTGS/KBr detector and ZnSe polarizer, operating in a range from 7500 to 400 cm^{-1} with a resolution of 4 cm^{-1}. Samples were measured with an orientation of 120 and 210° relative to the c-axis. Ultraviolet-Visible-Near infrared spectra were collected through SYSTEM SPECTROMETER GEMLAB GGTL, using a Xenon source in the range of 245 to 1050 nm.

X-ray diffraction (XRD) studies of a representative sample (EC_01) were performed to obtain a diffraction pattern characteristic of Cunas. The sample was first washed with distilled water, then dried and grounded to obtain 2 µm size particles. These studies were performed on a Carl Zeiss goniometer, model URD-6; the data were processed using the APX-61 AJ4 E LClS1 software, 8.4 version.

Major and trace elements of the twenty-five emeralds were determined by Energy Dispersive X-ray Fluorescence (EDXRF); a PANalytical Epsilon 5 spectrophotometer was used. This instrument has a side window tube of Sc/W with a maximum power of 600 W and a generator tube up to 100 kV, which allows the excitement of the K lines of heavy elements. Additionally, it has a Ge detector cooled to 77 K, and secondary targets of Al, Ti, Fe, Ge, Zr, Mo, Ag and Al_2O_3. Quantification was made via the Fundamental Parameters Method with a maximum of 20 iterations. Beryllium concentration (as oxide) was added manually; the value was obtained from the average data provided by Groat *et al.* (2008) for Colombian samples.

Double polished thin sections of selected samples (EC_02, EC_05, EC_08, and EC_09) were elaborated to conduct microthermometry analysis. The heating and cooling routine was performed through a Chaix-Meca-MTM 85 stage at the University of São Paulo. The average rate for cooling and heating was 3-5° Celsius per minute or even slower when required. The grouping of fluid inclusions assemblages was carried out following the criteria of Roedder (2002). Fluid and mineral inclusions were analyzed through Raman spectroscopy. The instrument was a Horiba LabRAM HR Evolution spectrometer with a 532 nm laser, coupled to an Olympus BX-41 microscope. The measurements were performed under 250 mW, 30 seconds of exposure, ten accumulation scans and 100% of laser intensity.

Photoluminescence spectra of the twenty-five emeralds were also acquired with the Horiba LabRAM HR Evolution equipment, with an acquisition time of 5s, accumulations of ten scans, a wavelength range from 660 to 700 nm, objective plan N 10x / 0.25 ∞ / - / FN22, reflection grid 1800 gr/mm, resolution 0.025 nm, a 532 nm laser, laser power 250 mW, power of excitation 0.5 mW, and a hole of 100 µm.

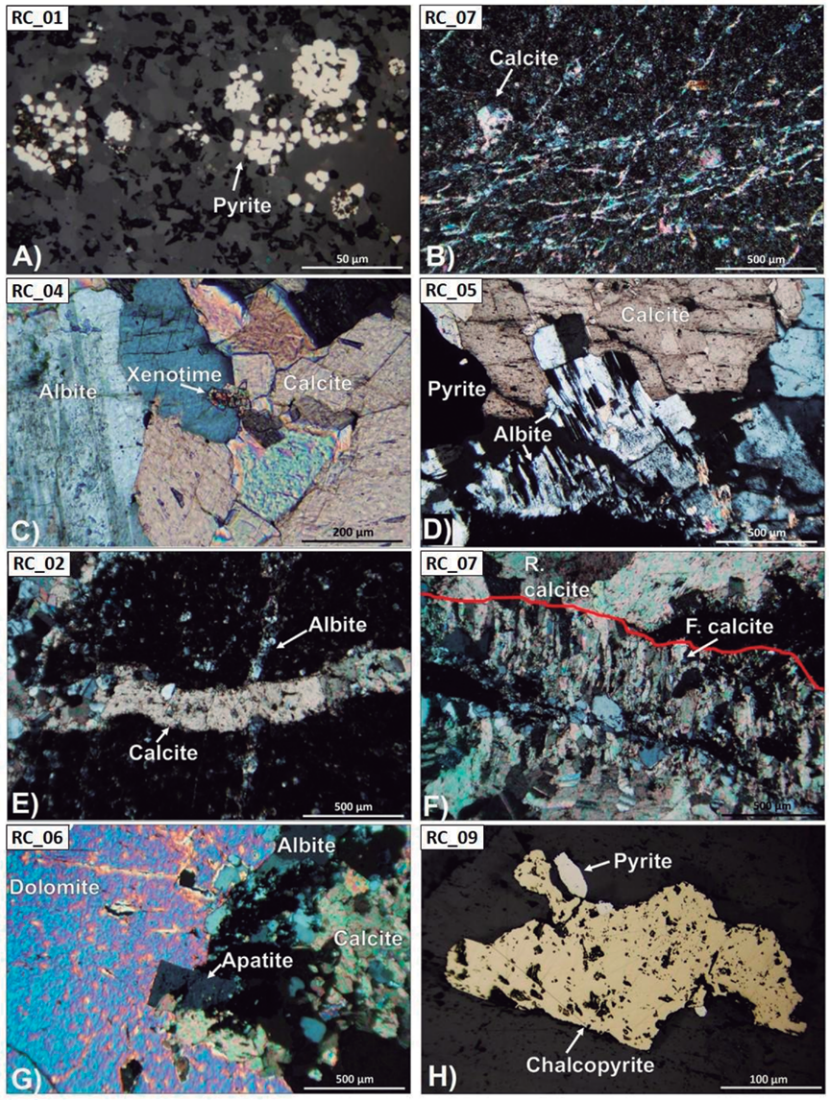

Figure 4. Photomicrographs of emerald veins from the Cunas mine. A) Framboidal pyrite from an organic-rich mudstone; PRL. B) Calcite veinlets crosscutting organic-rich mudstone. The host rocks commonly display strong hydrothermal alteration —carbonatization—; XPL. C) Close-up view of an intersection between an albite — xenotime vein and a vein dominated by rhombohedral calcite; XPL. D) Twined albite crystals which are partially replaced by calcite; XPL. E) Black shale where cross-cut relationships are noticeable. Albite veinlets are cross-cut by calcite; XPL. F) Vein showing two generations of carbonates (F. calcite: fibrous calcite; R. calcite: rhombohedral calcite), which grew under distinct regimes; XPL. G) Albite—fluorapatite vein in contact with later carbonates. Note the albite crystals are highly corroded by dolomite replacement; XPL. H) Tiny fragments of sulfides are occasionally found; these include pyrite, chalcopyrite, and sphalerite; PRL. Abbreviations: PPL: plane-polarized light, XPL: cross-polarized light, PRL: polarized reflected light.

Results

Mineralogy

The Cunas mineralization is related to hydrothermal veins and breccia zones (Figure 3B), which extend more than 90 meters deep from the surface. The pithead is located on the Furatena Formation, and the productive zones are only found in the middle layers of the Muzo Formation. Emerald-bearing veins are intimately associated with zones of intensive and overlapped hydrothermal alteration, predominantly albitization and carbonatization.

The host rocks of the mineralization may vary between calcareous mudstones, siltstones and black shales; their organic content is typically high and planar lamination is the most prevalent sedimentary structure. These rocks are mostly black or dark gray (Figure 3B, C, D, E); however, some variations may arise as a result of changes in composition and grain size. The main observed constituents are mica, plagioclase, quartz, framboidal pyrite, and minor monazite, tourmaline, and rutile (Figure 4A). Some white to gray fragments of albitized evaporites were locally observed. In the mineralized zones, the original host rock composition can be difficult to decipher due to the strong hydrothermal alteration and the small grain size (Figure 4B).

Four hydrothermal/mineral paragenesis stages can be recognized. The first stage consists of albitization of the host rock. Albite crystals are found in drusiform veinlets and breccias together with sporadic xenotime and fluorapatite (Figure 4C, D, E). Secondly, antitaxial veins of fibrous calcite are observed in certain areas; these veins are usually re-opened and intersected by later events (Figure 4F). The third mineral assemblage is dominated by white calcite, dolomite, muscovite, and quartz (Figures 3C, D, E and Figure 4G). This is the most predominant stage and is widely observed in the mine. The host rocks underwent strong carbonatization and an intensive brecciation; most of the minerals grew in open spaces so that euhedral crystals are very common. Calcite is found within the veins and breccias displaying rhombohedral and more complex crystallographic habits; dolomite is usually gray in color and rhombohedral in shape (Figure 3F). Less common minerals include vanadium-rich muscovite, pyrite, fluorapatite, rutile, tourmaline, albite, chalcopyrite, and sphalerite (Figure 4H). Emeralds occur exceptionally in pockets and pods associated with dolomite, “peach skin” calcite, quartz, parisite-(Ce), and fluorite (Figure 5A, B, D, E); bitumen fragments can also be found (Figure 5C).

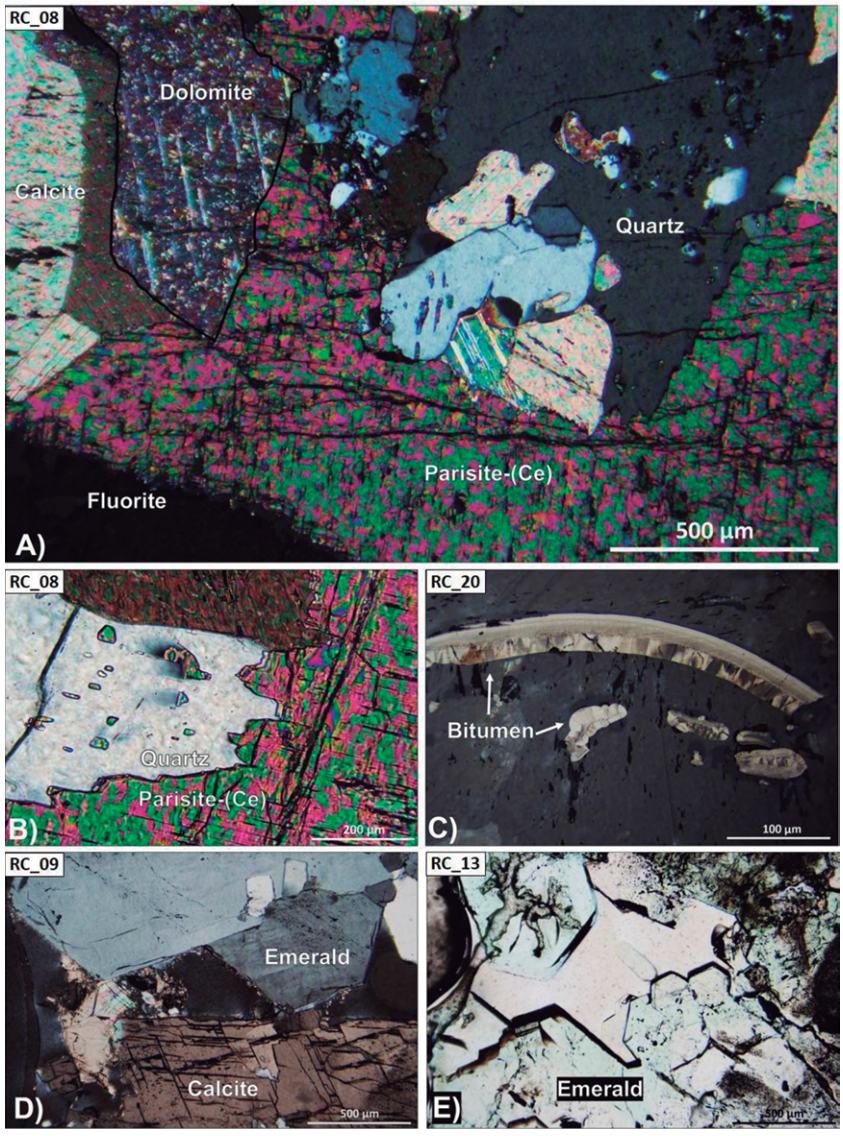

Figure 5. Photomicrographs of emerald veins from the Cunas mine. A) Indicative mineral assemblage from an emerald-bearing zone. Note the three carbonates (calcite, dolomite, and parisite-(Ce)) occur together; fluorite and quartz are often coarse and colorless; XPL. B) Intergrowing texture exhibited by parisite-(Ce) and quartz; XPL. C) Bitumen fragments surrounded by calcite; PRL. D) Common exemplar of hexagonal emerald and rhombohedral calcite. Note the euhedral forms occur as a result of open-space filling; XPL. E) Hexagonal emerald crystals found in a vug; PPL. Abbreviations: PPL: plane-polarized light, XPL: cross-polarized light, PRL: polarized reflected light.

In some cases, the emerald crystals are mildly fractured by post-mineralization deformation or covered by a thin film of late-stage calcite. Mineral specimens from the Cunas mine are highly valuable for collectors since they usually consist of euhedral emerald crystals on a black or white matrix (Figure 6).

The veins width ranges between 10 to 40 centimeters and their orientation is generally N25E dipping 40° and up to 90° eastwards. The breccia zones are generally thicker than the veins, and made up of clasts of previous veins, fragments of carbonaceous matter, and fault gouge. Finally, the fourth hydrothermal stage is characterized by irregular late-stage calcite that infills open spaces growing as a thin film on previously formed minerals. Replacement textures are very common —e.g. calcite after albite (Figure 4D, G)— and the identification of hydrothermal alteration assemblages can be highly problematic due to the overlapping of events and the re-opening of veins. The obtained samples from productive zones always displayed the four hydrothermal stages, whereas the samples taken from barren veins lacked at least one of the mineral assemblages. According to the petrographic relationships, a paragenetic sequence was established for the mineralization (Figure 7).

Figure 6. Photograph displaying a classic mineral specimen from the Cunas mine. The emerald crystals are usually euhedral and hexagonal; white calcite and light-grey dolomite are the commonest gangue minerals.

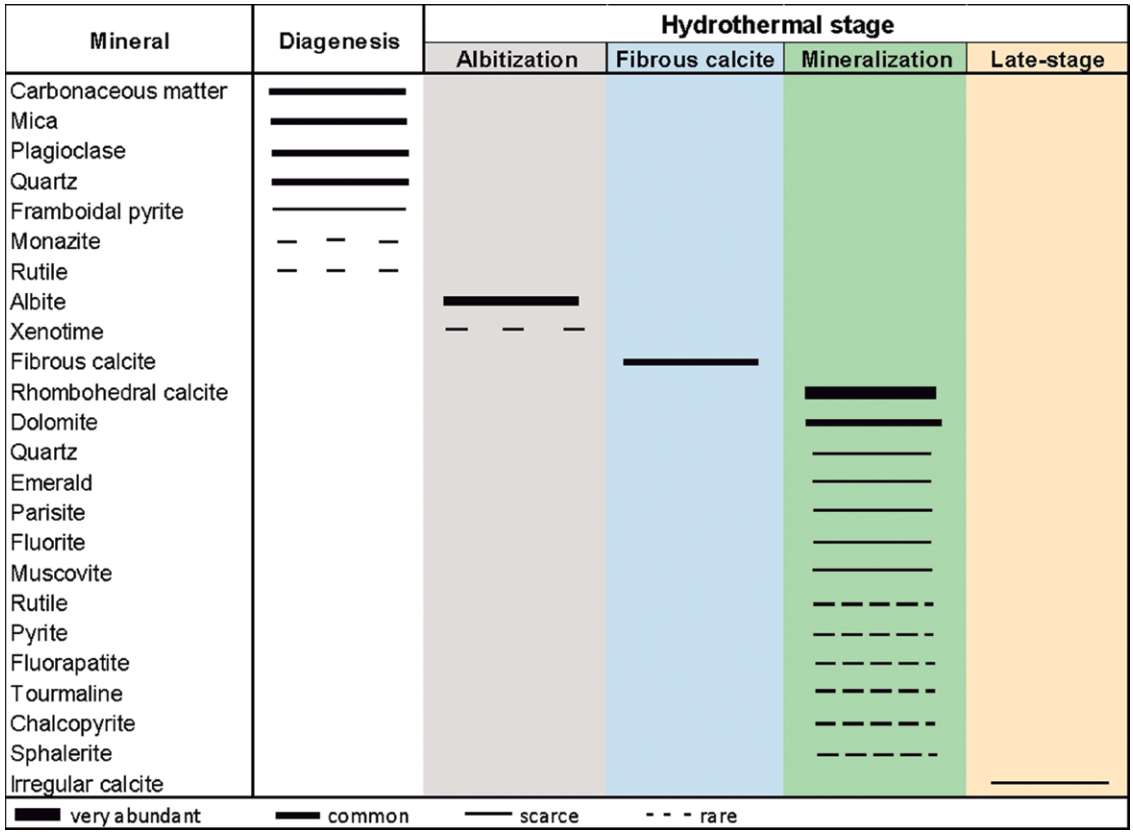

Figure 7. Generalized paragenetic sequence for the Cunas mineralization.

Gemological aspects

Emerald crystals typically occur as hexagonal prisms with basal pinacoids, sometimes double-terminated (Figure 3F and Figure 8A); stepped growing patterns are occasionally observed. Most of the samples have color zoning both parallel and perpendicular to the c-axis, where the core is light green and the rim has a higher color saturation (Figure 8A). Euhedral crystals also exhibit color zoning parallel to the growing c-axis. Dichroism is subtle and ranges between yellowish-green (perpendicular to the c-axis) to bluish-green (parallel to c-axis). Cut stones display a deep green hue and remarkable luster (Figure 8B).

Optically, the crystals show uniaxial behavior with low birefringence and negative optical character. The mean refractive index of the ordinary ray (n_ω) is 1.585, whereas for the extraordinary ray (n_ε) is 1.575. These values fall in the range of most Colombian emeralds, and approximate to those from the Coscuez mine. The estimated birefringence is 0.010. Table 1 shows average values of refractive index, birefringence, and density for Colombian emeralds, other world deposits and some synthetic emeralds.

Emeralds show moderate to weak red fluorescence under 365 nm ultraviolet light. Some samples fluoresce intensively according to their color saturation (Figure 8C, D). Reaction under the Chelsea filter is weak (red color), except for one sample (EC_16) that reacts strongly due to its high color saturation and its lack of fissures and inclusions. Solid inclusions are uncommon and mostly consist of albite, dolomite and lesser calcite, rutile, and black shale fragments.

Spectroscopic features

The obtained FT-IR spectra is characteristic of Colombian emeralds (Cedeño et al., 2015; Karampelas et al., 2019; Branca et al., 2019). Type I and II water absorption are observed, with the presence of CO_2 in 2358 cm^{-1} (Figure 9A). The range between 3200 and 7500 cm^{-1} presents absorption caused by Type I and Type II water stretching (Rondeau et al., 2008; Wood & Nassau, 1968). Absorption signals in 3555, 3647, 3610, 3629, 3694, 3697,

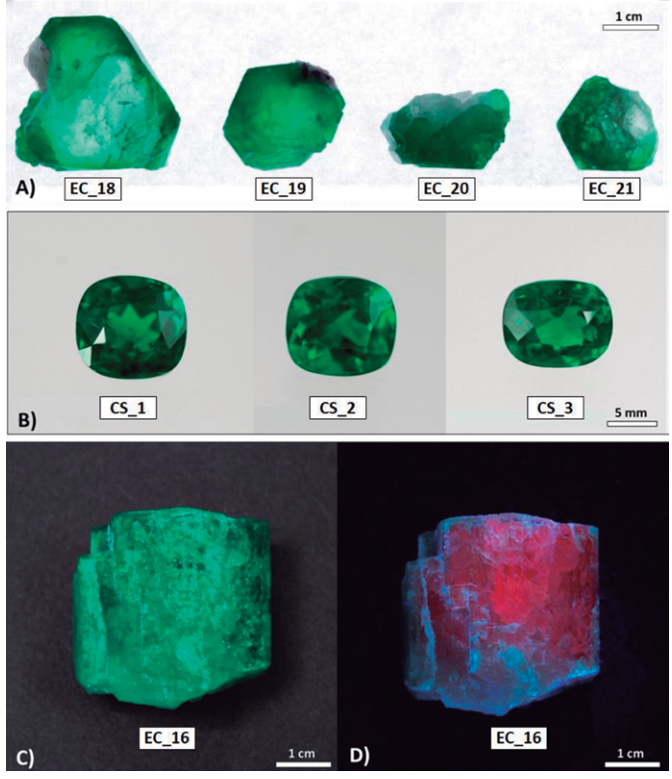

Figure 8. Photographs of Cunas emeralds. A) Hexagonal crystals displaying color zoning. B) Typical "deep-green" cut emeralds. C) Emerald crystal observed under normal light, D) The same crystal observed under ultraviolet light (365 nm), the red fluorescence is due to the chromium content.

Table 1. Comparative chart showing the refractive index, birefringence, and the density (specific gravity) of some natural and synthetic emeralds from literature.

Deposit	n_ε	n_ω	Birefringence	Density (g/cm^3)	References
Australia					
Poona	1.573	1.578	0.005-0.006	2.693	Zylberman, 1988
Brazil					
Faz. Bonfim	1.581-1.582	1.586-1.588	0.005-0.007	2.720	Zwaan et al., 2012
Carnaíba	1.582	1.588	0.006	2.720	Zylberman, 1988
Paraná	1.580-1.583	1.590	0.007-0.010	nd	Araújo Neto et al., 2019
India					
Ajmer	1.588	1.595	0.007	2.735	Zylberman, 1988
Colombia					
Muzo	1.564	1.57	0.006	2.70	Romero, 1993
Coscuez	1.578	1.584	0.006	2.609	Romero, 1993
Chivor	1.565	1.571	0.006	2.730	Romero, 1993
Yacopí	1.569	1.579	0.01	2.704	Romero, 1993
Pacho	1.570	1.576	0.006	2.70	Romero, 1993
Cunas	1.575	1.585	0.01	2.70	This study
Mozambique					
Murrua (Melela)	1.585	1.593	0.008	2.680	Gubelin, 1998
Norway					
Eidsvoll	1.579	1.587	0.008	2.75	Rondeau et al., 2008
Austria					
Habachtal	1.584	1.591	0.007	2.734	Zylberman, 1988
Pakistan					
Mingora	1.5887	1.5963	nd	2.777	Zylberman, 1988
Zambia					
Miku	1.582	1.589	nd	2.738	Zylberman, 1988
Kabufu	1.592	1.602	nd	2.770	Zwann et al., 2005
Zimbabwe					
Mayfield	1.584	1.590	nd	2.720	Zwann et al., 1997
Sandawana	1.584	1.590	nd	2.750	Zwann et al., 1997
Tanzania					
Manyara See	1.578	1.585	0.007	2.720	Gubelin, 1998
South Africa					
Gravelotte	1.583	1.594	nd	2.750	Gubelin, 1998
Russia					
Tokowaya (Ural, Sverdlovsk)	1.571	1.578	0.007	2.678	Gubelin, 1998
Canada					
Yukon	1.581	1.588	0.007	2.730	Groat et al., 2002
Synthetic - Hydrothermal					
Leichleitner	1.575	1.581	nd	2.649	Zylberman, 1988
Synthetic - Flux					
Chatham	1.573	1.578	0.005	2.650	Zylberman, 1988
Synthetic - Hydrothermal					
Russian	1.578	1.579	nd	2.730	Koivula et al., 1996
Synthetic - Hydrothermal					
Biron	1.569	1.573	0.004	2.710	Kane et al., 1985

3698, 1542, 1602-1550 and 1605 cm^{-1} correspond to Type I water (Wood & Nassau 1968, Cedeño et al., 2015). Absorption signals in 3592, 3597, 3655, 3660, 3654, 1628 and 1637-1630 cm^{-1} are due to Type II water. At 2813 cm^{-1}, a small band due to the presence of chlorine is found (Figure 9B, D) (Rondeau et al., 2008; Cedeño et al., 2015). Besides, less intense peaks are observed in the range from 2800 cm^{-1} to 2600 cm^{-1}, which have been assigned to partially deuterated water (HOD) and totally deuterated water (D_2O), more precisely, the bands situated at 2814, 2695, 2685, 2671 and 2640 cm^{-1} (Figure 9B) (Wood & Nassau 1968, Cedeño et al., 2015).

In general, Colombian emeralds exhibit two absorption bands due to electronic transitions of Cr^{3+} and V^{3+}. These two metallic ions isomorphically replace the Al^{3+} ion presented in beryl, giving the characteristic green color of emeralds (Bosshart, 1991; Schwarz, 2009). Collected UV-Vis-NIR spectra from Cunas emeralds show significant absorption signals due to V^{3+} and Cr^{3+} in 427, 607, 611, 636, and a doublet in 680-683 nm (Figure 10A) (Rondeau et al., 2008; Karampelas et al., 2019; Saeseaw et al., 2019). Additionally, a slight shoulder in 390 nm due to V^{3+} is observed (Schwarz, 2015). A small peak in 957 nm is observed due to the second overtone of OH groups or water molecules (Henderson *et al.,* 2015).

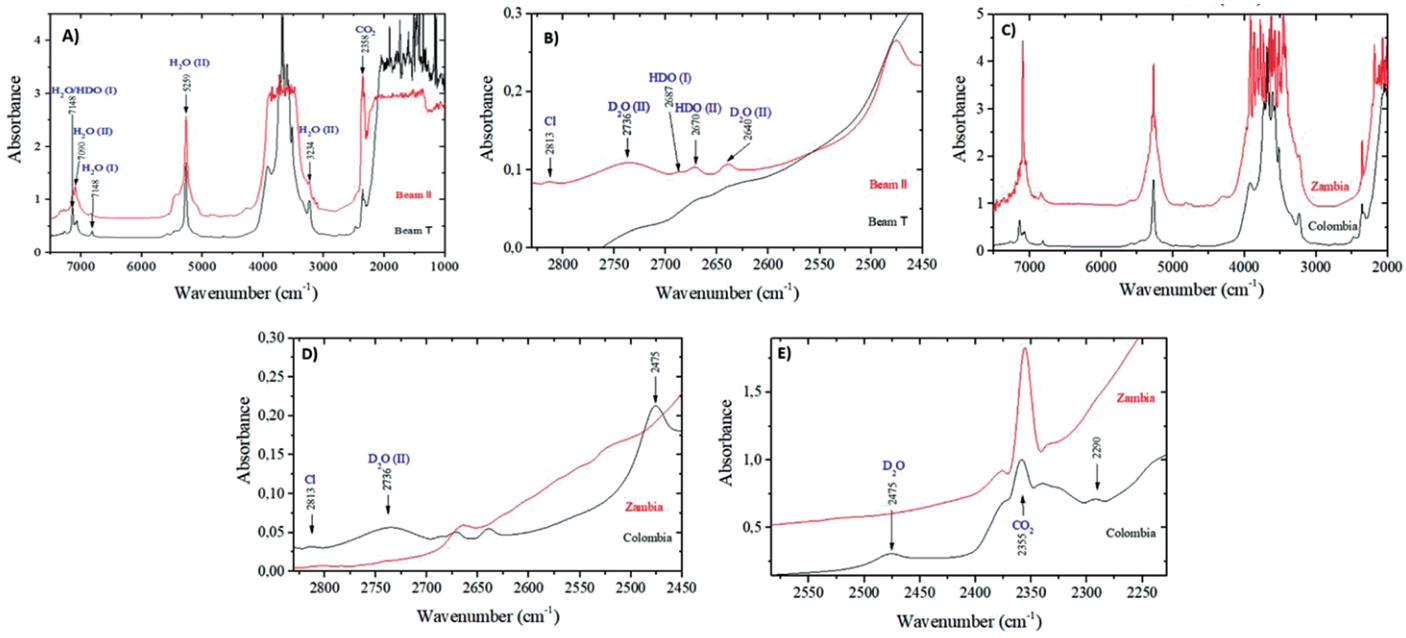

Figure 9. FT-IR absorption spectra. For A)-B) the spectra were collected with an incident beam parallel to c-axis (Beam II) and perpendicular to c-axis (Beam T). A) Typical spectra for Cunas emeralds at 1000 — 7500 cm^{-1}; the main observed bands correspond to CO_2, Type I —H_2O(I)— and Type II —H_2O(II) — waters. B) Close-up view at 2450 — 2850 cm^{-1} displaying partially deuterated water (HOD), and totally deuterated water (D_2O), and chlorine (Cl). C)-D)-E) Spectral comparison of the Cunas emeralds (Colombia) and Zambian emeralds. C) Typical signals at 1000 — 7500 cm^{-1} D) Close-up view at 2450 — 2850 cm^{-1}. E) Close-up view at 2250 — 2550 cm^{-1} showing the CO_2 and D_2O absorption bands.

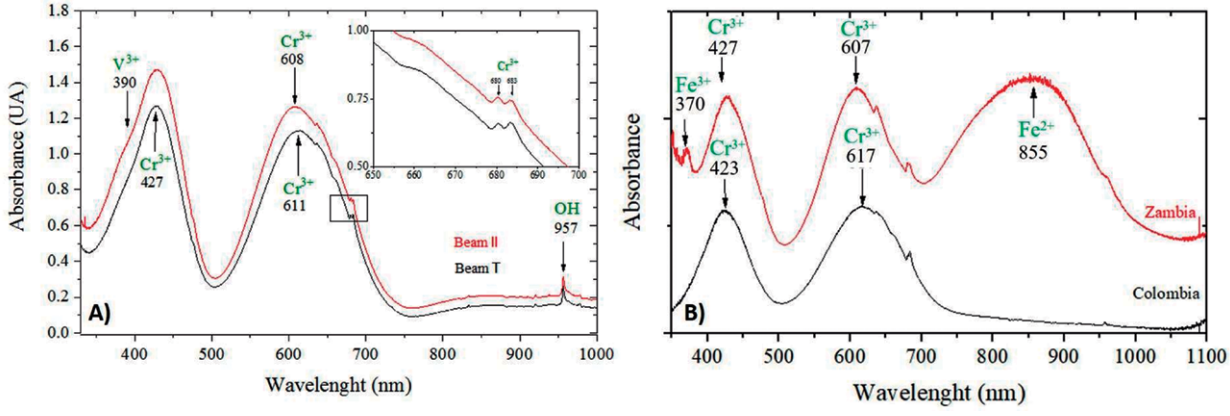

Figure 10. UV-Vis-NIR absorption spectra. A) Typical spectra from a Cunas emerald displaying V3+ and Cr3+ absortion bands. Note the absence of Fe2+ and Fe3+ absorption features. The spectra were collected with an incident beam parallel to c-axis (Beam II) and perpendicular to c-axis (Beam T). B) Spectral comparison of typical emerald from Cunas (Colombia) and a sample from Zambia. Note the Colombian spectra is Fe^{3+}-free. The upper spectra has been vertically offset for clarity.

Figure 11 shows the Raman spectra of beryl and CO_2 trapped in the fluid inclusions. Negligible differences can be observed between emeralds from Cunas and other Colombian localities. The average values obtained for the Fermi diad in Cunas are 1387.82 and 1284.89 cm^{-1}; in contrast to 1387.82 and 1284.89 cm^{-1} for Chivor and 1387.82 and 1284.89 cm^{-1} for Muzo (Cedeño *et al.*, 2015).

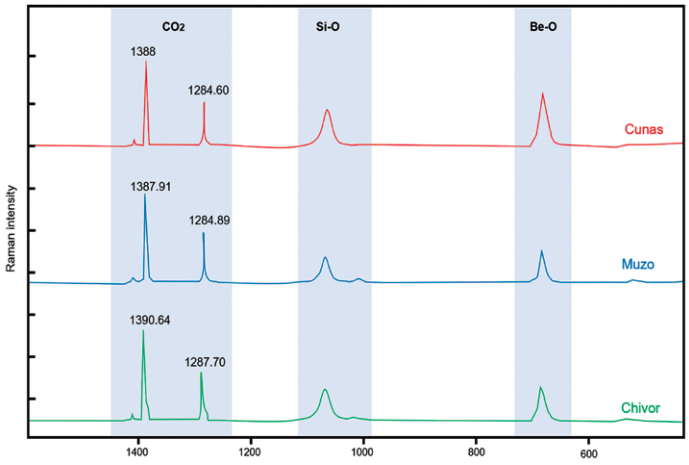

Figure 11. Comparative Raman spectra of Colombian emeralds showing three distinct zones. CO_2: corresponds to the Fermi Doublet signal of CO_2 from the gas phase of the fluid inclusions. Si-O: indicates a silicon-oxygen bond. Be-O: indicates a beryllium-oxygen bond, a typical signal from the host mineral (beryl). Note the Cunas Fermi doublet exhibits the longest separation. Y-axis is not to scale.

X-ray Diffractometry

X-ray diffraction results show no significant variations in the unit cell parameters of Cunas emeralds compared to other Colombian deposits (Table 2). The a_0 and c_0 values are 9.20788 ± 0.003 Å and 9.18420 ± 0.001 Å; the estimated volume is 673.3120.

Table 2. Unit cell parameters of emeralds from the main Colombian mines. *Taken from Romero (1993).

Mine	a_0 (Å)	c_0 (Å)	Volume (Å)
Muzo*	9.19204 ± 0.005	9. 7466 ± 0.001	671.4739
Coscuez*	9.20356 ± 0.003	9.19192 ± 0.008	674.2923
Chivor*	9.20710 ± 0.003	9.17432 ± 0.001	673.3243
Yacopí*	9.20767 ± 0.005	9.17022 ± 0.001	673.3024
Cunas (this study)	9.20788 ± 0.003	9.18420 ± 0.001	673.3120

Mineral chemistry

Representative FRX data are shown in Table 3. The chemical composition of Cunas emeralds is dominated by silica and alumina amounting in total ~80 wt%; the beryllium content was not measured, and a reference value was taken from Groat *et al.* (2008). The sum of magnesium, calcium, sulfur and alkali metals (Na, K) oxides stands for ~5.26 wt%; chlorine values average 2040 ppm, and its occurrence might be related to the water content. The most abundant trace elements are vanadium (average 8619 ppm), chromium (average 6462 ppm), iron (average 1039 ppm), and scandium (average 736 ppm). Other minor trace elements detected include Ni, Cu, Zn, Ga, Rb, Cs, Ti, and Mn.

The average V/Cr ratio is 1.33 and iron concentrations are relatively low, which represents typical values for emeralds from the Colombian Western Emerald Belt (Cedeño et al., 2015). Vanadium is the dominant chromophore, followed by chromium, and lesser iron; V-Cr-Fe relative proportions were plotted in a ternary diagram and compared with the whole spectrum of Colombian emeralds composition (Figure 12) (Cedeño *et al.* 2015). The relatively high chromium content and the low iron concentrations might explain the red fluorescence effect under ultraviolet light.

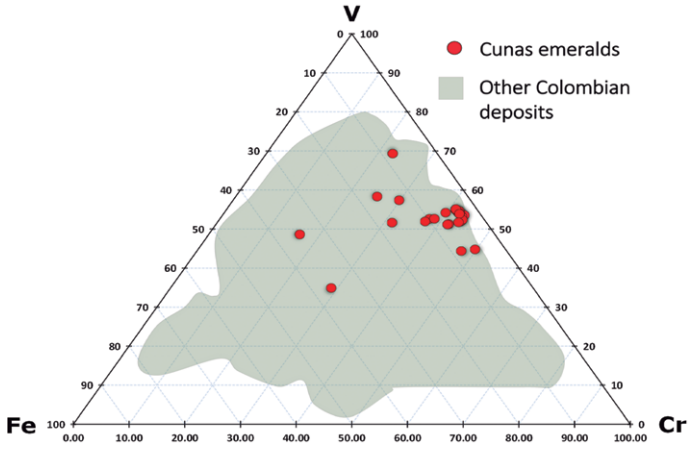

Figure 12. Ternary diagram of the Fe —Cr — V system. The red dots indicate samples from the Cunas mine; the gray field shows the entire spectra reported for Colombian emeralds from Cedeño et al. (2015).

Photoluminescence

The chromophore elements —chromium, vanadium, and iron— absorb part of the visible spectrum; this absorbed energy can eventually emerge again as a luminescence phenomenon. For the case of chromium, two spectral bands can be detected through photoluminescence (PL) analysis: R1 ~683 nm, and R2 ~680 nm (Wood, 1965), whose intensity and location depend on the chromium concentration and the Cr/Fe ratio; the higher the ratio the higher the spectral intensity (Nassau, 1978).

The R1 position for the Cunas emeralds varies from 683.67 nm to 683.98 nm, and its intensity can reach more than 6000 counts. The R2 position is well-defined and occurs as a small shoulder. Figure 13 exhibits the PL spectra of samples from Cunas, Chivor, Pakistan, and Zambia; and Figure 14 shows the Cr/Fe ratio versus R1 plot. Colombian emeralds range between 683.4 and 683.9 nm (Thompson *et al.,* 2017; García-Toloza *et al.*, 2019). In contrast, samples from Pakistan and Zambia range between 684.2 nm and 684.8 nm; Chivor emeralds range from 683.55 nm to 683.65 nm, and their average iron concentration is 800 ppm, which is notably lower than Cunas ~1039 ppm; the iron content of Zambian and Pakistan emeralds is higher than 14,000 ppm. The chromium content varies slightly between each locality (García-Toloza *et al*., 2019).

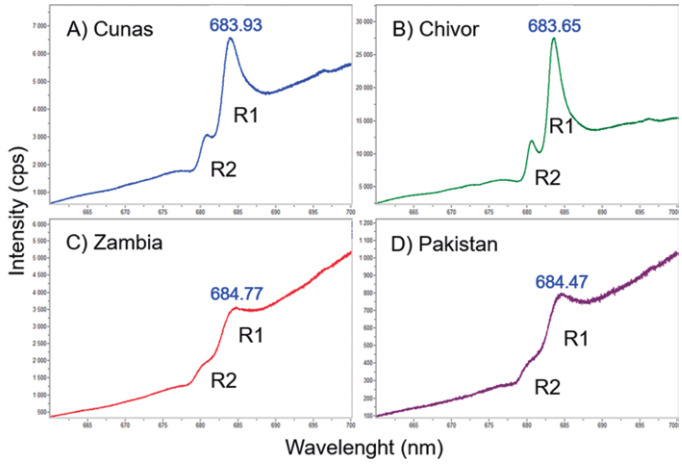

Figure 13. Photoluminescence spectra of selected emeralds from Colombia, Zambia, and Pakistan. The Colombian spectra display a higher intensity (6,000-25,000) in comparison to Zambia (3,500) and Pakistan (800). Spectra were collected with the excitation laser light aligned perpendicular to the c—axis of the crystal. cps: counts per second.

Table 3. X-ray fluorescence results for the Cunas emeralds. *Be: the beryllium content was taken as a theoretical number from Groat et al., (2008). bdl: below detection limit

MAJOR AND TRACE ELEMENTS FOR EMERALDS FROM THE CUNAS MINE																									
Oxide (wt%)	EC_01	EC_02	EC_03	EC_04	EC_05	EC_06	EC_07	EC_08	EC_09	EC_10	EC_11	EC_12	EC_13	EC_14	EC_15	EC_16	EC_17	EC_18	EC_19	EC_20	EC_21	EC_22	EC_23	EC_24	EC_25
BeO*	13.15	13.15	13.15	13.15	13.15	13.15	13.15	13.15	13.15	13.15	13.15	13.15	13.15	13.15	13.15	13.15	13.15	13.15	13.15	13.15	13.15	13.15	13.15	13.15	13.15
SiO_2	68.56	67.57	67.09	66.93	66.35	64.48	67.78	67.67	67.84	67.01	69.80	60.04	64.63	63.90	53.96	71.36	69.57	66.53	70.54	67.56	69.00	70.03	59.19	67.36	64.81
Al_2O_3	12.92	12.68	14.41	12.64	13.57	12.94	12.99	12.71	13.33	15.14	14.66	15.80	19.85	17.74	18.17	13.09	14.82	13.93	12.23	12.71	13.99	13.67	11.25	14.49	13.65
MgO	2.85	2.69	3.15	2.47	bdl	3.68	3.01	2.95	2.96	bdl	bdl	6.71	0.55	bdl	10.47	0.58	0.16	0.05	1.71	2.48	0.11	0.37	1.85	bdl	3.64
Na_2O	1.60	bdl	0.39	2.11	3.63	3.12	0.83	1.05	0.01	2.07	bdl	2.25	bdl	3.27	2.46	1.05	1.22	4.20	bdl	1.29	0.68	0.63	bdl	2.83	bdl
CaO	0.10	0.01	0.09	0.06	0.12	0.23	0.02	0.04	0.24	0.25	0.03	0.02	0.03	0.29	0.03	0.05	0.23	0.38	0.13	0.18	0.24	0.43	10.90	0.11	0.14
K_2O	0.07	0.05	0.14	0.11	0.24	0.20	0.07	0.11	0.05	0.07	0.06	0.07	0.04	0.12	0.06	0.14	0.10	0.13	0.06	0.16	0.18	0.13	0.11	0.26	0.29
SO_3	0.05	0.01	0.10	0.06	0.21	0.24	0.05	0.12	0.04	0.09	0.08	0.04	0.12	0.05	0.04	0.15	0.04	0.07	0.10	0.22	0.18	0.07	0.07	0.13	0.66
Total %	99.31	96.16	98.50	97.53	97.26	98.04	97.90	97.81	97.62	97.77	97.78	98.08	98.37	98.51	98.35	99.57	99.29	98.43	97.90	97.75	97.53	98.48	96.51	98.32	96.34
Trace (ppm)																									
V	11000	10820	8100	11530	12130	8110	10000	10570	11890	9880	10280	9020	6510	5160	7170	730	2430	6220	10430	10010	11080	6150	13190	5890	7170
Cr	8550	8770	2650	8890	9110	6610	8120	8300	8880	8300	8570	7100	7240	5530	6010	246	1482	5070	7660	7180	8110	4420	5740	3070	5930
Fe	724	591	895	692	818	1064	660	665	795	820	750	596	758	904	664	504	762	838	777	1236	1251	855	2477	878	5001
Sc	1047	915	858	1037	1093	1023	951	869	1036	915	958	815	462	330	773	65	327	489	792	686	713	811	976	222	242
Cl	992	878	1904	2020	3680	1836	784	1045	721	1325	963	1305	705	2180	799	2280	1448	2290	766	2260	2330	2200	9610	5970	711
Ni	5	2	8	4	13	5	7	4	9	15	13	18	46	36	40	2	7	6	2	2	4	21	1	13	7
Cu	14	12	17	14	20	22	12	15	13	20	19	17	48	43	32	18	14	22	75	376	341	105	57	75	1610
Zn	127	16	28	35	36	37	53	24	40	538	170	30	102	113	72	56	52	178	18	26	25	21	58	76	76
Ga	63	57	72	58	67	68	57	52	63	66	55	46	54	38	42	50	77	67	65	60	71	78	72	53	66
Rb	7	8	9	6	9	9	7	7	7	9	7	8	bdl	bdl	7	7	6	9	6	8	8	8	13	8	10
Cs	31	bdl	bdl	bdl	bdl	bdl	bdl	bdl	bdl	bdl	bdl	bdl	bdl	bdl	bdl	bdl	bdl	bdl	19	19	23	12	56	bdl	18
Ti	bdl	bdl	bdl	37	13	169	bdl	17	bdl	bdl	bdl	bdl	bdl	33	bdl	28	58	16	bdl	32	25	66	164	70	124
Mn	bdl	bdl	bdl	bdl	bdl	bdl	bdl	bdl	bdl	bdl	bdl	bdl	bdl	38	bdl	bdl	bdl	38	bdl	bdl	bdl	bdl	817	bdl	177

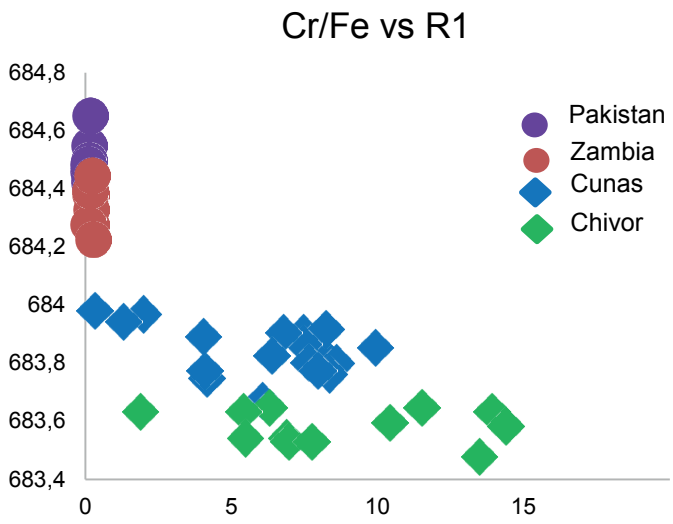

Figure 14. Cr/Fe vs. R1 plot. The R1 axis represents the maximum peak (wavelength). Samples from the Eastern Emerald Belt (green diamond) have high Cr/Fe ratio and exhibit shorter wavelength, while Cunas samples (blue diamond) have medium to low Cr/Fe ratio and exhibit longer wavelength. On the other hand, samples from Pakistan (purple dot) and Zambia (red dot) have a very low Cr/Fe ratio and exhibit much longer wavelengths.

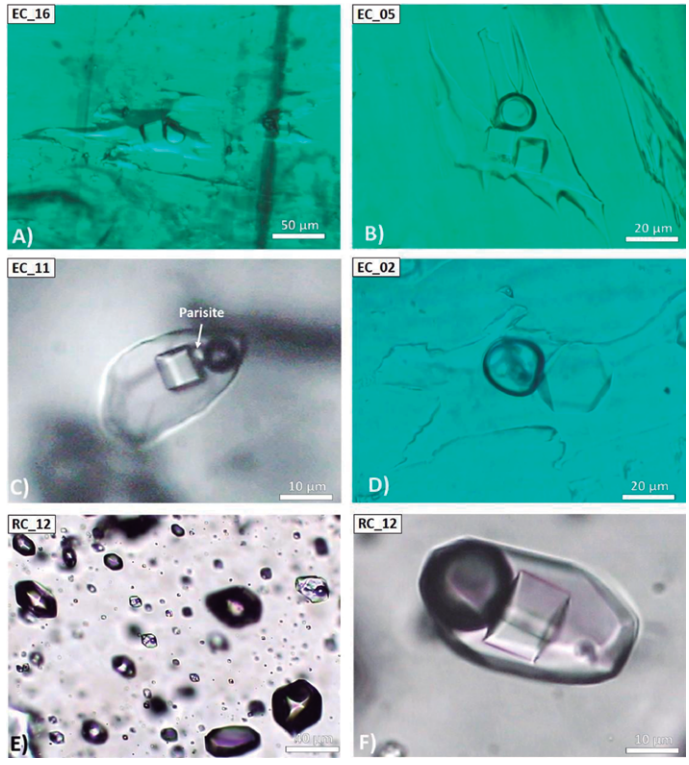

Figure 15. Photomicrographs of fluid inclusions. A) Emerald-hosted polyphase inclusion occurring in a jagged-edge cavity. B) Typical emerald-hosted fluid inclusion consisting of two daughter crystals, a liquid brine, and CO_2 (both liquid and gas). C) Emerald-hosted primary inclusion displaying the typical four phases; one of the daughter crystals was identified as parisite-(Ce). D) Emerald-hosted inclusion with sylvite(?) daughter crystal. E) Quartz-hosted primary inclusions. Note the entrapment is highly heterogeneous. F) Quartz-hosted inclusion consisting of a liquid brine, a daughter crystal —halite—, and a CO_2-N_2-CH_4-rich gas bubble

Fluid inclusions

The most common fluid inclusions trapped in the Cunas emeralds are poly-phase inclusions, containing two solids, liquid, and gas (Figure 15A, B, C, D). Their shape and orientation are variable, and two main groups can be distinguished. The inclusions are trapped in irregular or jagged cavities, which can reach outstandingly large sizes —more than 500 µm of diameter— (Figure 15A, B, D), and typically show necking down and leakage processes. Most of the fluid inclusion assemblages are oriented parallel to the c-axis or to a growing plane so that they are considered primary or pseudo-secondary. On the other hand, we grouped oval-shaped inclusions, whose size ranges approximately from 5 to 200 µm (Figure 15C). These FIAs are also regarded as primary, but they are less abundant, and show negligible evidence of necking down or leakage.

At room temperature, all the emerald-hosted fluid inclusions consist of a liquid-rich phase (70-75%v) with vapor (10-15%v) and two daughter crystals (10-15% v). In large-size inclusions was possible to observe two concentric rings conforming the bubble, indicating the coexistence of liquid and vapor CO_2 (Figure 15B); liquid CO_2 can account for ~3% of the inclusion volume. The daughter crystals are generally salts, predominantly halite; sylvite was also identified —based on crystal morphology upon cooling as noted by Ordóñez (1993)— and less abundantly calcite, dolomite, and parisite-(Ce). Abundant three-phase inclusions, consisting of an aqueous solution, one daughter crystal and a gas bubble, are widely found in gangue minerals, e.g., quartz, calcite, dolomite, parisite-(Ce), fluorite, fluorapatite, and albite (Figure 15E, F). Raman analysis in quartz-hosted inclusions identified CO_2, N_2, and CH_4; in emerald-hosted inclusions, only CO_2 could be detected, N_2 and CH_4 estimations were not suitable due to the high spectra saturation of the host beryl in the range where these compounds are visible (2000-3100 cm^{-1}).

The fluid inclusions whose arrangement was non-parallel to the c-axis were regarded as secondary. These are typically located in planes derived from re-healed fissures; most of them show evidence of leakage and necking down processes, this might also be caused by their large size. Some fluid inclusions hosted by associated quartz or carbonates are slightly different in shape, as they commonly occur as negative crystals; furthermore, CO_2-bearing inclusions were observed in quartz coexisting with liquid-rich inclusions, thus indicating heterogeneous trapping (Figure 15E). Tabular-shaped two-phase inclusions, consisting of liquid and vapor, were also sporadically found in calcite and dolomite.

The results of microthermometry analysis of emerald-hosted fluid inclusions are summarized in Table 4, and graphically shown in Figure 16. The first noticeable change in the system was observed in the range of -66 to -45°C;

Table 4. Microthermometric results of primary emerald-hosted fluid inclusions. Abbreviations: T-eut: eutectic point temperature; Tf-CO_2: temperature of melting point of CO_2; Tff-ice:final melting temperature of ice; T-ffhy: hydrohalite melting temperature; Th-CO_2: temperature of homogenization of liquid CO_2; Th: total vapor bubble homogenization temperature —gas to liquid—; Tm-NaCl: halite dissolution temperature; T-decrep: decrepitation temperature.

	T-eut (°C)	Tf-CO_2 (°C)	Tff-ice (°C)	T-ffhy (°C)	Th-CO_2 (°C)	Th (°C)	T-decrep (°C)	Tm-NaCl (°C)	Salinity (wt% NaCl eq.)
n	42	57	57	15	57	57	33	57	57
Mean	-56.2	-56.6	-29.6	-21.7	26.1	211.4	350.0	352.9	40.5
σ	6.7	0.6	4.0	2.4	1.5	14.9	14.5	16.6	1.8
MIN	-66	-58.9	-35.4	-25.1	23.9	190	340	335	38.6
MAX	-45.6	-55.9	-23.7	-19.1	28.6	230	380	380	43.4

this temperature is interpreted to be the eutectic point (Figure 16A). Due to the abundant CO_2 —both liquid and gas— it was possible to observe the melting point at ~-56.6°C (Figure 16B); the values reported below this point may suggest the presence of other compounds with lower melting temperatures. The final melting point of ice varies between -35 to -23°C (Figure 16C), and hydrohalite melting was observable at ~-21.6°C (Figure 16D). Some difficulties may occur when observing these phase changes, especially the metastability of the highly saline fluids. Homogenization of liquid CO_2 —change from liquid to gas state— was detected averaging at 26.13°C (Figure 16E); these results were used to determine the density of CO_2. According to the experimental diagrams by Shepherd (1985), a value of 0.2 g/cm³ was calculated. The total homogenization of the vapor bubble ranges from 190 to 230°C (Figure 16F), progressive heating led to the decrepitation or implosion of some inclusions; this occurred from 340 to 380°C (Figure 16H).

The salt —halite— dissolution took place from 335 to 380°C (Figure 16G); other daughter minerals like carbonates did not dissolve at temperature < 400°C. Based on the dissolution point of halite, the weight percentage of salinity —NaCl equivalent— was calculated through the program AqSo2e.exe by Bakker (2003); the values range from 38% to 43%. Likewise, the trapping conditions of the inclusions were estimated by the intersection of the H_2O-NaCl line with an isochoric path. The H_2O-NaCl line was defined in terms of the calculated salinity and the homogenization temperature. The isochoric area was established by the approximate hydrostatic and lithostatic gradients used by Cheilletz *et al.* (1994). Figure 17 shows two plots with the calculations of salinity, pressure, and homogenization temperature for the emerald-forming fluids. The minimum and maximum trapping pressure estimations correspond to 850-2420 bar, whereas temperature ranges from 256 to 337°C; the estimated density averages 1.068 g/cm³.

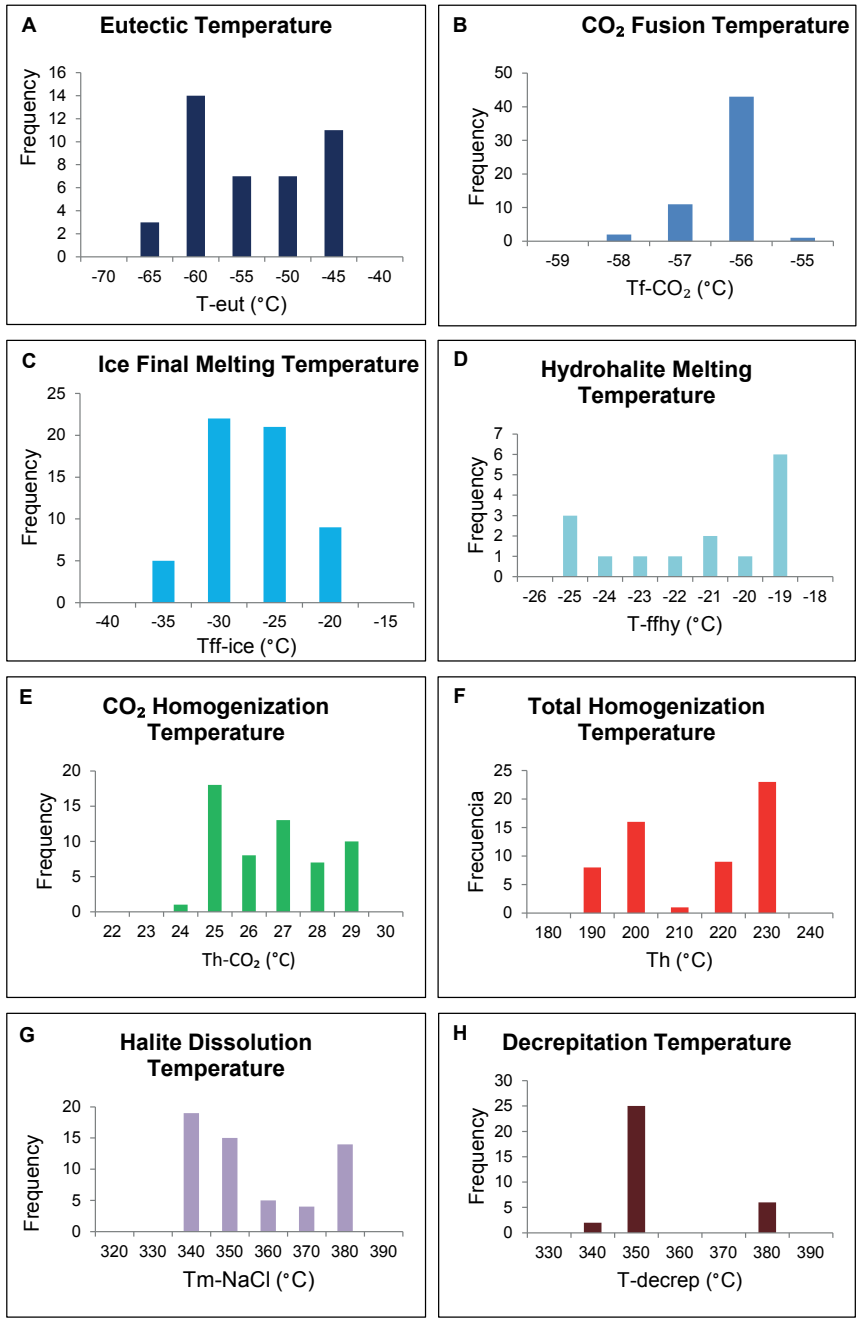

Figure 16. Histograms showing the microthermometric data. A) Eutectic point temperature (T-eut). B) CO_2 first melting temperature (Tf-CO_2). C) Final melting temperature of ice (Tff-ice). D) Hydrohalite melting temperature (T-ffhy). E) Temperature of homogenization of liquid CO_2 (Th-CO_2). F) Total vapor bubble homogenization temperature (Th). G) Halite dissolution temperature (Tm-NaCl), H) Decrepitation temperature (T-decrep).

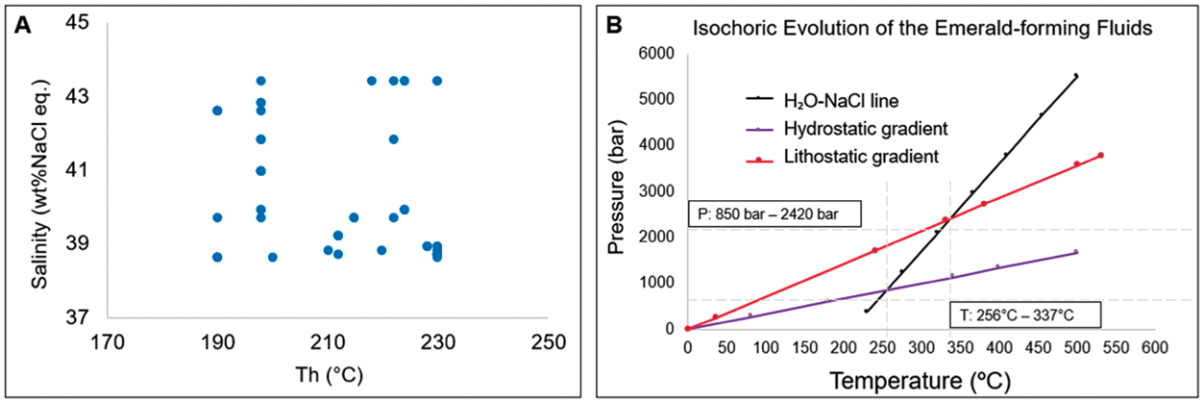

Figure 17. Plots showing microthermometric calculations. A) Salinity (wt% NaCl eq.) versus non-corrected homogenization temperature (Th). B) Isochoric evolution of the emerald-forming fluids. Minimum and maximum values for trapping conditions are listed (P: pressure, T: temperature).

Discussion

Geological similarities with other Colombian deposits

The geological setting of the Colombian emerald deposits has been extensively studied; at the Western Emerald Belt, multiple authors have proposed that the mineralization is stratabound — exclusively associated to Lower Cretaceous series from the Muzo and Rosablanca Formations— and epigenetic, i.e., formed by the circulation of non-magmatic hydrothermal fluids through structurally favorable sites where emerald formation can take place (Cheilletz *et al.*, 1994; Ottoway *et al.*, 1994; Giuliani *et al.*, 2000; Reyes *et al.*, 2006; Mantilla *et al.*, 2007; Terraza 2019).

According to the authors cited above, a simplified list of essential factors that can lead to a Colombian-type emerald mineralization would include these three aspects:

1) Stratigraphy: the mineralization is always linked to certain lithostratigraphic units. The emerald-hosting rock sequences particularly contain evaporitic levels or relicts after hydrothermal modification. These rocks are presumably the source of the main ingredients to form emeralds, i.e., Be, Cr, V, Al, Si, and associated elements like lanthanides, Ca, Na, K, Fe, S, P, F, and Cl.

2) Hydrothermal activity: hydrothermal fluids constitute the carriers of ligands and metals that can eventually react and crystallize as emeralds. Those fluids must contain specific chemical components under special P-T conditions. The action of hydrothermal fluids is evidenced in field as hydrothermal alteration, vein-infill with indicative mineral assemblages, and geochemical anomalies at different scales.

3) Structural control: it is critical for the focusing and promoting of fluid mixing and precipitation. Effective structural traps lead to a high rate of fluid-rock interaction, generation of cavities, and consequently accumulation of gem-quality emeralds.

Regarding the first factor, the Maripí district is located no further than 6 kilometers from the Muzo area, and the emerald mineralization lies on the same lithostratigraphic unit —the Muzo formation—. This was first noted by Reyes *et al.* (2006). In the Cunas Mine, the productive zones are found in calcareous mudstones and siltstones (Figure 3B, C, and D). These rocks are remarkably organic-rich and contain rare earth elements (REE) authigenic minerals such as monazite, two chemical components thoroughly involved in the mineralizing processes (Giuliani *et al.*, 2000; Verbel 2017).

Two particular rock types are described by Cheilletz *et al.* (1996) in the Muzo, Coscuez and Chivor mineralized zones: whitish albitites (*Kaolin*) and stratiform tectonic breccias (*Cenicero*). We observed gray albitites in the vicinity of some productive areas. These rocks are commonly interpreted as the product of intensive Na metasomatism of evaporite horizons (Giuliani *et al.*, 2000; Branquet *et al.*, 2015). In contrast, Cenicero zones were not observed. Stratiform tectonic breccias occur as a result of concomitant faulting and fluid flowing (Branquet *et al.*, 1999, 2015). Therefore, the presumed absence of these breccias would probably be related to a structural condition, instead of the lack of hydrothermal activity.

In terms of hydrothermal activity, multiple pieces of evidence of fluid-derived minerals are here documented (Figure 3, Figure 4, Figure 5, Figure 6). The fluid composition estimated upon primary fluid inclusions reveals no major changes with results reported for other Colombian deposits (Figure 17). Time-pressure conditions fall in the range of Colombian-type emeralds (Kozlowski et al., 1988; Giuliani et al., 1990, 1995; Cheilletz et al., 1994, Ottoway et al., 1994; Romero, 1993, 1998; Romero et al., 1999; Banks et al., 2000; Mantilla et al., 2007; Toloza, 2017), and the fluid composition is dominated by common components, i.e., Na+, Ca^{2+}, K+, Cl- and CO_2.

The high salinity values —38-42 wt% NaCl eq.— have been associated with the involvement of evaporite-derived fluids, whereas the Na-Ca dominated composition is explained by the mixing of two fluids (Giuliani *et al.*, 1995; Romero 1998; Banks *et al.*, 2000). In the Maripí area, carbonates from the La Pita, Españoles, and the Cunas mine were examined through oxygen and carbon isotopic studies, yielding a non-magmatic source and a hybrid isotopic signature (Niño, 2017). This indicates strong similarities with the isotopic fingerprints for other Colombian districts where a magmatic input has been ruled out intensely (Cheilletz *et al.*, 1994).

In general, the mode of occurrence of the Cunas mineralization is similar to other Colombian deposits; the emeralds are hosted by veins and breccias in hydrothermally altered zones. Albitization and carbonatization are ubiquitous and typical of productive areas (Figure 4). These features are critical given that Na-Ca metasomatism plays a key role in the location of beryl accumulation (Beus et al., 1972; Kozlowski et al., 1988; Romero 1993, 1998; Banks et al., 2000). The mineral association consisting of emerald-calcite-parisite-(Ce)-fluorite is a common feature at the Muzo mines (Ottoway et al., 1994; Giuliani et al., 2000; Banks et al., 2000), and it was repeatedly observed in Cunas (Figure 3, Figure 5); bitumen was also observed as embedded fragments in hydrothermal veins (Figure 5C). The presence of organic compounds — bitumen and CO_2-CH4-N_2 in the fluid inclusions— may suggest the emerald-forming fluids reacted with the organic-rich wall-rocks, especially through thermochemical sulfate reduction processes. According to Giuliani et al., (2000), this mechanism plays a key role as it promotes the leaching of beryllium from the black shales. However, in Cunas, hydrothermal pyrite is scarce and no H_2S was detected in the fluid inclusions. An alternative explanation is that the parental brines were sulfate-poor, a fact that would require further isotopic testing. Common chemical components expressed as mineral assemblages and fluid inclusions agree with a classical Colombian-type mineralization.

Three paragenetic stages can be objectively differentiable in most of the mining districts (Cheilletz *et al.*, 1996; Giuliani *et al.*, 2000; García-Toloza *et al.*, 2018; González-Duran *et al.*, 2019). At the Cunas mineralization, similar mineral assemblages have been described; nevertheless, our observations point to a system where at least four stages can be distinguished (Figure 7). Two possibilities could explain this situation. i) The lack of a detailed mineral description in the other mines, especially highlighting the complexity of differentiating between the very same minerals, e.g., fibrous, rhombohedral and irregular calcite. ii) A slightly different fluid evolution that gave rise to a multi-stage system. Although no significant differences can be addressed

in terms of fluid composition, specific wall-rock interactions could have led to subtle changes in the cooling paths of the ore-forming fluids; as a result, a set of different mineral textures would form as a consequence of multiple episodes of crystallization. We consider these two options are plausible; most of the previous studies have focused on the understanding of major features from a regional perspective. Few documents, describing specific mines, are available. On the other hand, particularities between Colombian emerald deposits are well-documented and roughly involve timing, tectonic setting, lithological and geochemical aspects of the mineralization (Romero 1993, 1998; Branquet *et al.*, 1999, Giuliani *et al.*, 2000; Pignatelli *et al.*, 2015; García-Toloza *et al.*, 2018).

It is noteworthy that during the carbonatization stage numerous minerals were formed (Figure 7), including silicates, carbonates, sulfides, phosphates, oxides, and F-rich phases as fluorite, parisite-(Ce) and fluorapatite. We think this occurs as a result of a series of factors prompted by a major process. These factors necessarily include: the input of additional chemical components, abrupt changes in P-T conditions that may trigger mineral precipitation, the availability of fluorine complexes for promoting effective transport of chemical components —beryllium and REE—. Our observations point to an abrupt change in fluid chemistry —and probably P-T conditions— due to fluid mixing; the lack of microthermometric data from every mineralizing state can limit this conclusion. However, Banks *et al.* (2000) stated that fluid mixing is certainly a process that exerts a strong influence in the availability of chemical components and consequent mineral precipitation. Undoubtedly, fluorine is a key ingredient in the chemical system as promotes beryllium mobility, an idea supported by the close association of emerald and fluorine-bearing minerals —fluorite, parisite-(Ce), and apatite—.

Finally, the structural setting of the Cunas mineralization is poorly constrained. However, some observations can be noted. In the northern Maripí area, a well-defined ~N30E trend controls the emplacement of emerald-bearing veins; this is well-documented in the La Pita mine by Puerto *et al.* (2012) and also in Cunas (García-Toloza *et al.*, 2018). Even though, there are no detailed observations about the style and origin of veins; a high rate of fluid-rock interaction is required, as the concentration of chromophore elements —Cr-V-Fe— is remarkably high and similar to the values from the Puerto Arturo mine in Muzo (Cedeño *et al.*, 2015). The abundance of solid inclusions within vein minerals —emerald, calcite, and dolomite— is a common feature at the Cunas mine, and might suggest an extensive interaction with the host rocks.

One noteworthy feature at the Cunas mine is the apparent absence of trapiche emeralds. This could be regarded as a structural issue, as trapiches are supposed to form exclusively at fault tips in fault-propagating anticline settings; Pignatelli *et al.* (2015) documented this mechanism in the Muzo area —the main deposit of trapiche emeralds in the world—. Interestingly, trapiche emeralds have been found in the La Pita mine, which is located a few hundred meters north of Cunas. This might suggest the structural positioning of the two deposits is slightly different. In Cunas, the main mineralization zones occur in a homocline configuration (Castaño *et al.*, 2019); whereas the occurrence of trapiche emeralds in the La Pita, would be possibly related to an anticline-related fault propagation zone. It is convenient to clarify that trapiche emeralds do not occur throughout the La Pita mine but are restricted to very small zones —fault tips—. Structural mapping of the entire area would be highly suggested to elucidate this topic. Another alternative would be the assumption that trapiche-emerald zones are still undiscovered at the Cunas mine.

Based on the previous observations, we propose that the emerald mineralization in the Cunas mine was originated by the same global processes that took place in Muzo and other Colombian districts. We do not find significant evidence to exclude extrapolation from the Muzo area to the Maripí district.

Distinctive features of the Cunas emerald

Gemological and mineralogical characteristics, as the refractive index, birefringence, unit cell parameters, and density, show no appreciable differences with reported values for emeralds from other Colombian deposits (Table 1, Table 2).

Cunas emeralds exhibit unit cell data with slight differences in comparison to the firstly reported values for beryl: $a_0 = 9.21 \pm 0.01$ Å and $c_0 = 9.17 \pm 0.01$ Å (Bragg & West, 1926). Radclife & Campbell (1966) proposed these differences may occur because of variations in the theoretical chemical composition e.g., aluminum (Al^{3+}) can be partially substituted by transition metals, especially the chromophores elements chromium, vanadium, and iron. The reported values in Table 3 indicate this took place, and consequently, the unit cell dimensions were modified.

Fourier-Transform Infrared absorption spectra of Cunas emeralds is characteristic of Colombian emeralds, especially those from the Western Emerald Belt (Cedeño *et al.*, 2015). Figure 9C, D, E shows a spectral comparison with emeralds from the Kafubu mine in Zambia. We found four main differences: the absence of deuterated water in 2736 cm^{-1} and 2475 cm^{-1}, chlorine in 2813 cm^{-1}, and a water-related band in 2290 cm^{-1} (Cedeño *et al.*, 2015; Karampelas *et al.*, 2019). Regarding UV-Vis-NIR spectra, the Zambian samples exhibit four main absorption bands (Figure 10B). A small band is observed in 370 nm due to Fe^{3+}. Three broadbands are observed in 420 nm, 610 nm are due to Cr^{3+}, and another broadband in 850 nm due to Fe^{+2} (Schwarz, 2009). In general, Colombian emeralds have a low concentration of iron species, this characteristic allows to separate Cunas emeralds from iron-rich deposits like Kafubu in Zambia (Karampelas *et al.*, 2019).

According to the results displayed in Figure 11, Raman analysis of CO_2 in fluid inclusions can help to discriminate emeralds from the two Colombian emerald belts (Jimenez, 2017). No significant differences with emeralds from Muzo were observed, thus indicating comparable CO_2 trapping conditions.

The concentration of chromophore elements in the Cunas emeralds is dominated by V (average 8619 ppm) > Cr (average 6462 ppm) > Fe (average 1039 ppm). This V-Cr-Fe ratio is similar to values reported for the La Pita (Maripí) and Puerto Arturo (Muzo) emeralds (Cedeño *et al.*, 2015; Jiménez, 2017). Cunas emeralds are iron-poor and fall in the range of reported values for Colombian emeralds (Figure 12). The vanadium-rich character of the emeralds may be related to the high organic content of the host rocks, as noted by García-Toloza *et al.* (2018). The low iron content is probably a reflection of a chemical system in which carbonates were effective collectors of iron. The role of pyrite as an iron collector is limited due to the low occurrence of sulfides.

The photoluminescence makes it possible to differentiate Colombian vanadium-rich emeralds, such as those from Cunas, to chromium-rich ones such as those from the Eastern Emerald Belt (Figure 14). Iron-rich emeralds —Zambia and Pakistan— can also be easily distinguished by the position and intensity of the R1 peak. Our data confirm that there is a distinct correlation between the R1 position and Cr/Fe ratio for each locality so that emeralds can be identified according to its provenance. This contrast derives from the respective geological setting; Cunas emeralds are hosted by sedimentary rocks and formed by low-temperature fluids; where Zambian and Pakistan emeralds are associated to magmatic processes which involved pegmatites and mafic-ultramafic rocks (Groat *et al*., 2008; Giuliani *et al.*, 2019).

Emerald-forming fluids

Microthermometry analysis indicates the emerald-forming fluids were trapped at relatively low temperature ~260-340°C and pressure ~850-2400 bar, with relatively high density —1.07 g/cm³—, elevated salinity 40.5 wt% NaCl eq., and CO_2-N_2-CH_4 as the main volatiles. Regarding the chemical composition of the aqueous phase, the estimation of the salinity is only an approximation as Na^+ is by any means the only dissolved ion. The low eutectic temperature and hydrohalite melting point suggest the presence of K^+, Ca^{2+}, Mg^{2+} (Chi & Ni, 2007; Roedder, 1984; Shepherd *et al.*, 1985). The daughter crystals are also indicative of the chemical composition as they are supposed to form as a result of isochoric fluid saturation after trapping. Halite, sylvite, calcite, dolomite argue for a rich input of Na^+, K^+, Ca^{2+}, and Mg^{2+}; whereas parisite-(Ce) —$Ca(Ce,La)_2(CO_3)_3F_2$— indicates the existence of rare earth elements (REE^{3+}), CO_2^{2-} and F^-. The microthermometric observations correlate with the main mineral phases found in the veins, e.g., albite, muscovite, calcite, dolomite, fluorite, fluorapatite, and parisite-(Ce). The replacement of albite by calcite (Figure 4D, E, G) is widespread and a meaningful feature at the Cunas mine; this texture suggests disequilibrium probably originated by mixing of two contrasting fluids. Romero (1993, 1998), Ordóñez *et al.* (1997), and Banks *et al.* (2000) examined the chemical components of fluid inclusions in Colombian emeralds and concluded fluid mixing was a critical factor for emerald precipitation. At Cunas, two deposit-scale hydrothermal events can be identified: albitization and carbonatization. On the one hand, the formation of albite requires high amounts of Na-rich fluids, i.e., highly saline fluids.

As previously noted, albitites are interpreted to be relicts of evaporitic layers (Giuliani *et al.*, 2000; Branquet *et al.*, 2015); therefore, the fluid responsible for albitization could have obtained elevated salinities from the dissolution of local evaporitic layers. On the other hand, the fluid responsible for carbonatization was Ca-rich as calcite is a common daughter crystal in fluid inclusions, and calcite is by far the commonest gangue mineral in the hydrothermal veins. This fluid was CO_2^{2-} and F^- rich so that effective extraction and remobilization of beryllium and REE from the country rocks took place (Banks *et al.*, 2000; Giuliani *et al.*, 1990, 1995, 2000; Kozlowski *et al.*, 1988). Primary two-phase —lacking salts as daughter crystals— inclusions in carbonates may indicate the salinity was significantly lower in comparison with the Na-rich fluid. Besides, the heterogeneous trapping of fluid inclusions in quartz suggests boiling, a process that might explain the wide variety of calcite crystal shapes. Regarding the source of the Ca-rich solution, as previously pointed out, Niño (2017) argues for a non-magmatic input and a hybrid isotopic signature, thus reinforcing the idea of fluid mixing. A basinal origin for Ca-rich fluids is highly suggested, where pore-fluids migrated and evolved through the strata.

Based on these data, we propose that the emerald mineralization at the Cunas mine was originated by the mixing of two hydrothermal fluids of different sources; one fluid was highly saline, derived from evaporite dissolution —as suggested by Romero *et al.* (1993); Banks *et al.* (2000)—, and was the responsible for the albitization of the host rocks; a second calcium-rich fluid evolved from connate waters and was equilibrated by the interaction with calcareous and organic-rich wall rocks —as evidence by CO_2-N_2-CH_4 in fluid inclusions—; this fluid could have been the responsible for the widespread carbonatization. As a result, emerald mineralization took place at structurally favorable places where fluid mixing was highly promoted.

The described geological and physicochemical features for the Cunas mine, are in agreement with an epigenetic sediment-hosted mineralization formed by the circulation and mixing of relatively low-temperature non-magmatic fluids; a highly accepted model for the Colombian emerald deposits. Fluid inclusions data are particularly similar to the reported range for Colombian emerald deposits (Banks *et al.*, 2000; Cheilletz *et al.*, 1994; Giuliani *et al.*, 1990, 2000; Kozlowski *et al.*, 1988; Mantilla *et al.*, 2007; Ottaway, 1994; Romero, 1993, 1998; Toloza, 2017).

Conclusions

At Cunas, emeralds occur as infill products in veins and breccias, consisting of calcite – dolomite – albite – quartz – parisite-(Ce) – fluorite – pyrite, hosted by organic-rich mudstones from the Muzo formation. There is also a close association between hydrothermal alteration —albitization and carbonatization— and mineralization.

Distinct spectroscopic techniques reveal the Cunas emeralds share common gemological features with other Colombian deposits, especially with those from the Western Emerald belt. Cunas emeralds are iron-poor and vanadium-rich, therefore they can be readily differentiated from non-Colombian iron-rich emeralds.

Microthermometry analysis indicates the emerald-forming fluids were trapped at similar conditions to other Colombian deposits, whose temperature ranges from 260°C to 340°C and pressure ~850-2400 bar, with relatively high density 1.06859 g/cm³, elevated salinity 40.5 wt.% NaCl eq., and a chemical system dominated by H_2O-NaCl-$CaCl_2$-KCl-$MgCl_2$, volatiles —CO_2-N_2-CH_4— and fluorocarbonate complexes.

Acknowledgements

We wish to thank the Universidad Nacional de Colombia staff for the research support. We acknowledge Esmeraldas Santa Rosa S.A. for the field and logistics support, especially Edwin Molina, Germán Forero, Ing. Alfonso Torres; the mine staff always treated us so warmly and we appreciate their kind attention during our visits to the mine facilities. Funding from the National Emerald Federation (Fedesmeraldas) was vital for the accomplishment of this research. Assistance from Camilo Sánchez (Green Shine C.I S.A.S.) and Orlando Rodríguez with data collection is also greatly appreciated. Contributions from Harry Vargas, Daniel Moncada, Leonardo Paipa and Andrés Martín helped to improve notably the manuscript. We also thank the anonymous reviewers for their constructive comments.

References

Acosta, J., Velandia, F., Osorio, J., Lonergan, L., & Mora, H. (2007). *Strike-slip deformation within the Colombian Andes.* Geological Society, London, Special Publications, 272, 303-319. https://doi.org/10.1144/GSL.SP.2007.272.01.16

Araújo Neto, J. F., Barreto, S. B., Müller, A. & Santos, L. C. M. L. (2019). Mineralogical and gemological characterization of emerald crystals from Paraná deposit, NE Brazil: a study of mineral chemistry, absorption and reflectance spectroscopy and thermal analysis. *Brazilian Journal of Geology,* 49(3), 1-15. http://dx.doi.org/10.1590/2317-4889201920190014

Bakker, R. J. (2003). Package FLUIDS 1. Computer programs for analysis of fluid inclusion data and for modelling bulk fluid properties. *Chemical Geology,* 194, 3-23.

Banks, D., Giuliani, G., Yardley, B., & Cheilletz, A. (2000). Emerald mineralisation in Colombia: fluid chemistry and the role of brine mixing. *Mineralium Deposita*, 35(8), 699-713.

Beus, A., & Mineev, D. (1972). *Some geological and geochemical features of the Muzo-Coscuez Emerald zone, Cordillera Oriental, Colombia.* United Nations Internal Report 1689, Ingeominas, Bogotá, Colombia.

Bosshart, G. (1991). Emeralds from Colombia (part 2). *Journal of Gemmology,* 22(7), 409-425.

Bragg, W., & West, J. (1926). *The structure of beryls, Be3Al2Si6O18*. Proceedings of the Royal Society of London, A(111), 91-714.

Branca, C., Arcovito, A., Cosio, E., Interdonato, M., Sabatino, G., Wanderlingh, U., & D'Angelo, G. (2019). Combining Fourier transform infrared and Raman spectroscopies with Gaussian deconvolution: An improved approach for the characterization of emeralds. *Journal of Raman Spectroscopy,* 1–9. https://doi.org/10.1002/jrs.5810

Branquet, Y., Laumonier, B., Cheilletz, A., & Giuliani, G. (1999). Emeralds in the Eastern Cordillera of Colombia: Two tectonic settings for one mineralization. *Geology,* 27, 597-600.

Branquet, Y., Giuliani, G., Cheilletz, A., & Laumonier, B. (2015). *Colombian Emeralds and Evaporites: Tectono-Stratigraphic Significance of a Regional Emerald-Bearing Evaporitic Breccia Level.* Proceedings of the 13th SGA Biennial Meeting SGA, 4, 1291-1294.

Castaño, O. S., González-Durán, A. F., García-Toloza, J., & Uribe, A. (2019). *Caracterización geológica, geoquímica y mineralógica de la mina Cunas en el municipio de Maripí.* XVII Colombian Geological Conference, Santa Marta, Colombia 147-149.

Cedeño, C., Herreño, M., Fortaleche, D., & Jimenez, J. (2015). *Progress on the study of Parameters related to the Origin of Colombian Emeralds.* Incolor Special Edition - Emerald, 88-97. https://www.gemstone.org/incolor/IncolorEmerald/index.html#88

Cheilletz, A. Féraud, G., Giuliani, G., & Rodríguez, C. (1994). Time pressure-temperature constraints on the formation of Colombian Emeralds: a laser probe and fluid inclusion study. *Economic Geology,* 89, 362-380.

Cheilletz, A., & Giuliani, G. (1996). The genesis of Colombian emeralds: A restatement. *Mineralium Deposita*, 31, 359-364.

Chi, G., & Ni, P. (2007). Equations for Calculation of NaCl/(NaCl+CaCl2) Ratios and Salinities form Hydrohalite- Melting and Ice-Melting Temperatures in the H_2O-NaCl-$CaCl_2$ System. *Acta Petrologica Sinica,* 23(01), 33-37.

Cooper, M. A., Addison, F. T., Alvarez, R., Coral, M., Graham, R. H., Hayward, A. B., Howe, S., Martinez, J., Naar, J., Peñas, R., Pulham, A. J., & Taborda, A. (1995). Basin development and tectonic history of the Llanos Basin, Eastern Cordillera and Middle Magdalena Valley, Colombia. *American Association of Petroleum Geologists Bulletin,* 79, 1421-1443.

García-Toloza, J., & González-Durán A. F. (2018). *Firma geoquímica y certificación de esmeraldas fase 1*. Non-published CDTEC technical report.

García-Toloza, J., Herreño-Daza, M. J., González-Durán, A. F., Cedeño-Ochoa, C. J., & Angarita-Sarmiento, L. G. (2019). *Photoluminescence analysis to determine the origin of emeralds from the Eastern and Western belts in Colombia.* Proceedings of the 15th Biennial Meeting SGA, Glasgow, Scotland, 2, 931-934.

Giuliani, G., Cheilletz, A., Dubessy, J., & Rodriguez, C. T. (1990). *Chemical composition of fluid inclusions in Colombian emerald deposits*. Proceedings of the Eighth Quadrennial IAGOD Symposium, Ottawa, Canada, 159-168.

Giuliani, G., Cheilletz, A., Arboleda, C., Carrillo, V., Rueda, F., & Baker, J. (1995). An evaporitic origin of the parent brines of Colombian emeralds: fluid inclusion and sulphur isotope evidence. *European Journal of Mineralogy,* 7(1), 151-166.

Giuliani, G., France-Lanord, C., Cheilletz, A., Coget, P., Branquet, Y., & Laumonier, B. (2000). Sulfate reduction by organic matter in Colombian emerald deposits: Chemical and stable isotope (C, O, H) evidence. *Economic Geology,* 95, 1129-1153.

Giuliani, G., Branquet, Y., Fallick, A. E., Groat, L., & Marshall, D. (2015). *Emerald deposits around the world, their similarities and differences.* InColor special issue, 56-69.

Giuliani, G., Groat, L. A., Marshall, D., Fallick, A. E., & Branquet, Y. (2019). Emerald Deposits: A Review and Enhanced Classification. *Minerals,* 9, 105.

González-Durán, A. F., García-Toloza, J., Bonilla-Osorio, G. E., Cedeño-Ochoa, C. J., & Angarita-Sarmiento, L. G. (2019). *Geology of the La Pava emerald mine, Colombia.* Proceedings of the 15th SGA Biennial Meeting Glasgow, Scotland, 2,901-904.

Groat, L., Marshall, D., Giuliani, G., & Murphy, D. (2002). Mineralogical and Geochemical study of the Regal Ridge Emerald showing, Southeastern Yukon. *The Canadian Mineralogist,* 40, 1313-1338.

Groat, L., Giuliani, G., Marshall, D., & Turner, D. (2008). Emerald deposits and occurrences: A review. *Ore Geology Reviews*, 34(1), 87-112.

Gubelin, E. J. (1988). La Présence D´émeraudes au Pakistan, La Vallée de Swat. L´émeraude. Connaissances actuelles et prospectives. *Association Française de Gemologie,* 185-192.

Henderson, G., Neuville, D., & Downs, R. (2015). *Spectroscopic Methods in Mineralogy and Materials Sciences.* Reviews in mineralogy and geochemistry, University of Toronto, Toronto, Canada, 200 pp.

Hewton, M. L., Marshall, D. D. Ootes, L., Loughrey, L. E. & Creaser, R. A. (2013). Colombian-style emerald mineralization in the northern Canadian Cordillera: Integration into a regional Paleozoic fluid flow regime. *Canadian Journal of Earth Sciences,* 50, 857–871.

Horton, B. K., Parra, M. & Mora, A. (2020). Construction of the Eastern Cordillera of Colombia: Insights from the sedimentary record. In: Gómez, J. & Mateus-Zabala, D. (Eds.) *The Geology of Colombia, Volume 3 Paleogene – Neogene.* Servicio Geológico Colombiano, Publicaciones Geológicas Especiales 37, 22 p. Bogotá. https://doi.org/10.32685/pub.esp.37.2019.03

Ingeominas, & Mora, A. (2005). *Levantamiento de Información estratigráfica y estructural de los cinturones esmeraldíferos de la cordillera Oriental.* Ingeominas Technical report BTA-013, Bogotá.

Kane, R. & Liddicoat, R. (1985). The Biron Hydrothermal Synthetic Emerald. *Gems & Gemology*, 21(3), 156-170.

Karampelas, S., Al-Alawi, A., Al-Shaybani, B., Mohamed, F., & Sangsawong, S. (2019). Emeralds from the most important occurrences: Chemical and spectroscopic data. *Minerals,* 9(9), 561. https://doi.org/10.3390/min9090561

Keith, J. D., Nelson, S. T., Thompson, T. J., Dorais, M. J., Olcott, J., Duerichen, E., & Constenius, K. N. (2002). The genesis of fibrous calcite and shale-hosted emerald in a nonmagmatic hydrothermal system, Uinta Mountains, Utah. *Geological Society of America,* 34, 55.

Koivula, J., Kammerling, R., DeGhionno, D., Reinitz, I., Fritsch, E., & Jhonson, M. (1996). Gemological investigation of a new type of Russian Hydrothermal Synthetic Emerald. *Gems & Gemology*, 32(1), 32-39.

Kozlowski, A., Metz, P., & Estrada, H. (1988). Emeralds from Somondoco Colombia: Chemical composition, (FI) and origin. *Neues Jahrbuch Mineralogie, Abhandlungern*, 159(1), 23-49.

Mantilla, L. C., Silva, A., Serrano, J. J., Conde, J., Gómez, C., Ramírez, J. C., Meza, J. A., Pelayo, Y., Ortega, L. M., Plata, L. M., & Peña, E. (2007). *Investigación petrográfica y geoquímica de las sedimentitas del Cretácico inferior (K1) y sus manifestaciones hidrotermales asociadas planchas 169, 170, 189, 190 (Cordillera Oriental), implicaciones en la búsqueda de esmeraldas.* INGEOMINAS-Universidad Industrial de Santander (UIS), Bogotá.

Marshall, D., Downes, P., Ellis, S., Greene, R., Loughrey, L., & Jones, P. (2016). Pressure–Temperature–Fluid Constraints for the Poona Emerald Deposits, Western Australia: Fluid Inclusion and Stable Isotope Studies. *Minerals,* 6(130), 2-22.

Mojica, J. (1995). Generalidades acerca de la geología de Colombia. *Geología Colombiana,* 20, 157-160.

Mora, A., Villagómez, D., Parra, M., Caballero, V. M., Spikings, R., Horton, B. K., Mora-Bohórquez, J. A., Ketcham, R. A., & Arias-Martínez, J.P. (2020). Late Cretaceous to Cenozoic uplift of the northern Andes: Paleogeographic implications. In: Gómez, J. & Mateus-Zabala, D. (Eds.) *The Geology of Colombia, Volume 3 Paleogene – Neogene.* Servicio Geológico Colombiano, Publicaciones Geológicas Especiales 37, p. 89-121. Bogotá. https://doi.org/10.32685/pub.esp.37.2019.04

Nassau, K. (1978). The origins of color in minerals. *American Mineralogist,* 63, 219-229.

Niño, G. F. (2017). *Geological and Geochemical Analyses for Emerald Exploration in the Muzo Formation along the Western Emerald belt, Colombia.* M.Sc. thesis, National Taiwan University.

Ortega, L. (2007). *Tipología y condiciones de formación de las manifestaciones del sector esmeraldífero "Peña Coscuez" (Municipio San Pablo de Borbur, Boyacá).* M.Sc thesis, Universidad Industrial de Santander, Bucaramanga.

Ottaway, T., Wicks, F., Bryndzia, L., Kyser, T., & Spooner, E. (1994). Formation of the Muzo hydrothermal emerald deposit in Colombia. *Nature,* 369, 552 – 554.

Pignatelli, I., Giuliani, G., Ohnenstetter, D., Mathieu, S., Mathieu, M., Morlot, C., & Branquet, Y. (2015). Colombian Trapiche Emeralds: Recent Advances in Understanding Their Formation. *Gems & Gemology,* 51(3), 222-259.

Puerto, J., Fernández, J., Pantorrilla, A. (2012). *Caracterización mineralógica y estructural de la mina de esmeraldas La Pita (Boyacá-Colombia).* B.Sc tesis, Universidad Nacional de Colombia, Bogotá.

Ordóñez, R. F., Rocha, B., Bello, R., Fuzikawa, K., & Svisero, D. (1994). Inclusões cristalinas e fases sólidas associadas as inclusões fluidas em esmeraldas da Colômbia. *Revista Escola de Minas, Ouro Preto,* 47(2), 128-133.

Ordóñez, R. F., Rocha, B., Bello, R., Fuzikawa, K., Svisero, D., & Scultz-Guttler, R. (1997) Composição, Origem e Significado geológico das Inclusões fluidas de esmeraldas das jazidas de Muzo, Pacho, Coscuez, Yacopí e Chivor, Colômbia. *Geochimica Brasiliensis*, 11(1), 001-021.

Radclife, D. & Campbell, F. (1966). Beryls from Birch Portage, Saskatchewan. *Canadian Mineralogist*, 8, 493-505.

Reyes, G., Montoya, D., Terraza, R., Fuquen, J., Mayorga, M., & Gaona, T. (2006). *Geología del Cinturón Esmeraldífero Occidental. Planchas 169, 170, 189 y 190.* Instituto Colombiano de Geología y Minería (INGEOMINAS).

Roedder, E. (1963). Studies of fluid inclusions II: Freezing data and their interpretation. *Economic geology,* 58(2), 167-211.

Roedder, E. (1984). The fluids in salt. *American Mineralogist,* 69, 413-439.

Roedder, E. (2002). *Fluid Inclusions, Encyclopedia of Physical Science and Technology.* Third edition 2, 71-77.

Romero, O. F. (1993). *Mineralogia, Inclusões fluidas e Gênese de esmeraldas das jazidas de Chivor, Coscuez, Muzo, Pacho e Yacopí, Colombia.* M.Sc thesis, Universidade de São Paulo, Instituto de Geociências, Sao Paulo.

Romero, O. F. (1998). *Esmeraldas Colombianas: Mineralogia, Geologia e Gênese.* Ph.D. thesis, Universidade de São Paulo, Instituto de Geociências, Sao Paulo.

Romero, O. F., & Hernández, O. (1999). Características Mineralógicas e Inclusiones Fluidas de las Esmeraldas del Municipio de San Antonio de Yacopí, Cundinamarca, Colombia. *Geología Colombiana*, 24, 149-158.

Romero, F. H., Schultz-Güttler, R., & Kawashita, K. (2000). Geoquímica del Rubidio-Estroncio y edad de las esmeraldas colombianas. *Geología Colombiana,* 25, 221-229.

Rondeau, B., Fritsch, E., Peucat, J., Nordrum, F., & Groat, L. (2008). Characterization of emeralds from a historical deposit: Byrud (Eidsvoll), Norway. *Gems & Gemology,* 44(2), 108-122.

Saeseaw, S., Renfro, N. D., Palke, A. C., Sun, Z., & McClure, S. F. (2019). Geographic Origin Determination of Emerald. *Gems and Gemology,* 55(4), 614-646.

Schwarz, D. (2009). Emeralds from the Silk Road Countries – A Comparison with Emeralds from Colombia. *InColor,* 12, 38-43.

Schwarz, D. (2015). *The Geographic Origin Determination of Emeralds.* Incolor Special Edition - Emerald, 98-105. https://www.gemstone.org/incolor/IncolorEmerald/index.html#88

Svadlenak, E. (2015). *Ar40/Ar39 Ages and trace element variations in Colombian emeralds.* B.Sc. tesis, Oregon State University, Corvallis.

Terraza, M. R. (2019). Notas sobre el contexto tectonoestratigráfico de formación de las esmeraldas colombianas. *Boletín Geológico,* 45, 37-48. https://doi.org/10.32685/0120-1425/boletingeo.45.2019.486

Thompson, D. B., Bayens, C. J., Morgan, M. B., Myrick, T. J., & Sims, N. E. (2017). Photoluminescence spectra of emeralds from Colombia, Afghanistan, and Zambia. *Gems and Gemology,* 53(3), 296-311. https://doi.org/10.5741/GEMS.53.3.296

Toloza, J. G. (2017). *Estudios de inclusiones fluidas en esmeralda Colombiana "Tras la firma química", Boyacá (Colombia).* B.Sc. thesis, Universidad Nacional de Colombia, Bogotá.

Valls, R. A. (2017) Technical Report on the 122-95M Emerald License in the Boyacá District, Colombia, http://www.furagems.com/uploads/Colombia-Technical-Report-by-Competent-Person.pdf (last accessed June 2020).

Van Der Hammen, T. (1958). Estratigrafía del Terciario y Maastrichtiano, continentales y Tectogénesis de los Andes de Colombia. *Boletín Geológico,* 6(1-3), 67-128.

Verbel, A. (2017). *Mineralogía de elementos de tierras raras en las mineralizaciones esmeraldíferas colombianas.* M.Sc thesis, Universidad Nacional de Colombia, Bogotá.

Wood, N., & Nassau, K. (1968). The Characterization of Beryl and Emerald by visible and infrared absorption spectroscopy. *The American Mineralogist,* 53, 777-800.

Zylberman, N. (1988). Tableu Synoptique comparatif des propriétés Gemologiques des Gisements Majeurs et des Principales synthèses. L´émeraude. Connaissances actuelles et prospectives. *Association Française de Gemologie,* 227-229.

Zwaan, J., Kanis, J., & Petsch, E. (1997). Update on Emeralds from the Sandawana Mines, Zimbabwe. *Gems & Gemology,* 33(2), 80-100.

Zwann, J., Seifert, A., Vrána, S., & Laurs, B. (2005). Emeralds from the Kafubu Area, Zambia. *Gems and Gemology,* 41(2), 2-34.

Zwaan, J., Dorrit, J., Häger, T., Cavalcanti, Neto, M., & Kanis, J. (2012). Emeralds from the Fazenda Bonfim Region, Rio Grande do Norte, Brazil. *Gems & Gemology,* 48(1), 2-17.